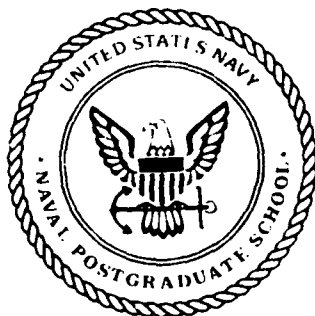


AD-A258 056



2

NAVAL POSTGRADUATE SCHOOL Monterey, California



S DTIC
ELECTE
DEC 17 1992
A **D**

THESIS

EXAMINATION OF THREE-DIMENSIONAL (3-D) EFFECTS
ON SOUND PROPAGATION THROUGH MESOSCALE
FEATURES USING 3-D COUPLED MODE THEORY

by

Jacqueline M. Binhlam

June 1992

Thesis Advisor:

Ching-Sang Chiu

Thesis Co-Advisor:

Laura L. Ehret

Approved for public release; distribution is unlimited.

92-31674



92 12 16 070

REPORT DOCUMENTATION PAGE				Form Approved OMB No. 0704-0188	
1a REPORT SECURITY CLASSIFICATION UNCLASSIFIED			1b RESTRICTIVE MARKINGS		
2a SECURITY CLASSIFICATION AUTHORITY			3 DISTRIBUTION/AVAILABILITY OF REPORT		
2b DECLASSIFICATION/DOWNGRADING SCHEDULE			Approved for public release; distribution is unlimited.		
4 PERFORMING ORGANIZATION REPORT NUMBER(S)			5 MONITORING ORGANIZATION REPORT NUMBER(S)		
6a NAME OF PERFORMING ORGANIZATION NAVAL POSTGRADUATE SCHOOL		6b OFFICE SYMBOL (If applicable)	7a NAME OF MONITORING ORGANIZATION NAVAL POSTGRADUATE SCHOOL		
6c ADDRESS (City, State, and ZIP Code) Monterey, CA 93943			7b ADDRESS (City, State, and ZIP Code) Monterey, CA 93943		
8a NAME OF FUNDING/SPONSORING ORGANIZATION		8b OFFICE SYMBOL (If applicable)	9 PROCUREMENT INSTRUMENT IDENTIFICATION NUMBER		
8c ADDRESS (City, State, and ZIP Code)			10 SOURCE OF FUNDING NUMBERS		
PROGRAM ELEMENT NO		PROJECT NO	TASK NO	WORK UNIT ACCESSION NO	
11 TITLE (Include Security Classification) Examination of Three-Dimensional (3-D) Effects on Sound Propagation Through Mesoscale Features Using 3-D Coupled Mode Theory					
12 PERSONAL AUTHOR(S) Binhlam, Jacqueline M.					
13a TYPE OF REPORT Master's Thesis		13b TIME COVERED FROM _____ TO _____		14 DATE OF REPORT (Year, Month, Day) June 1992	
				15 PAGE COUNT 79	
16 SUPPLEMENTARY NOTATION					
17 COSATI CODES			18 SUBJECT TERMS (Continue on reverse if necessary and identify by block number)		
FIELD	GROUP	SUB GROUP			
			Underwater sound propagation modeling		
19 ABSTRACT (Continue on reverse if necessary and identify by block number)					
<p>A study of the three dimensional (3-D) effects of mesoscale variability on underwater sound propagation is conducted by interfacing the Chiu-Ehret 3-D acoustic coupled mode (CM) model with a forecasted sound speed field generated by the Harvard Open Ocean Model (HOOM). This research concentrates on the sensitivity of the acoustic wave field to source depth and location with respect to a core ring in the Gulf Stream system for a 50 Hz sound source.</p> <p>The inclusion of the exact 3-D physics in acoustics modeling requires substantial computer resources. For this reason, it is very desirable to determine when the simpler adiabatic or Nx2-D approximations may be used. To achieve this goal, "exact" 3-D acoustic coupled mode model calculations are compared to results from the adiabatic approximation and Nx2-D approximation in terms of transmission loss and phases and amplitudes of individual mode modulation envelopes. The results show that the accuracy of the adiabatic and Nx2-D approximations depend strongly on the radial and transverse sound speed gradients along the track and the acoustic quality considered.</p>					
20 DISTRIBUTION/AVAILABILITY OF ABSTRACT <input checked="" type="checkbox"/> UNCLASSIFIED/UNLIMITED <input type="checkbox"/> SAME AS RPT <input type="checkbox"/> DTIC USERS			21 ABSTRACT SECURITY CLASSIFICATION		
22a NAME OF RESPONSIBLE INDIVIDUAL Ching-Sang Chiu			22b TELEPHONE (Include Area Code) 408-646-3239		22c OFFICE SYMBOL 68 Ci

Approved for public release; distribution is unlimited

Examination of Three-Dimensional (3-D) Effects on Sound Propagation Through
Mesoscale Features Using 3-D Coupled Mode Theory

by

Jacqueline M. Binhlam
Lieutenant, U.S. Navy
B.S., United States Naval Academy, 1982

Submitted in partial fulfillment of the
requirements for the degree of

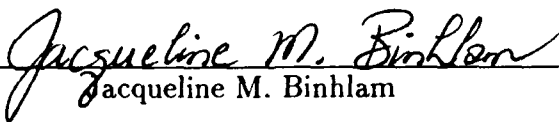
MASTER OF SCIENCE IN
METEOROLOGY AND PHYSICAL OCEANOGRAPHY

from the

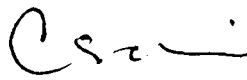
NAVAL POSTGRADUATE SCHOOL

June 1992


Author:



Jacqueline M. Binhlam

Approved by:


Ching-Sang Chiu, Advisor

Approved by:


Laura L. Ehret, Co-Advisor


Curtis A. Collins, Chairman
Oceanography

ABSTRACT

A study of the three dimensional (3-D) effects of mesoscale variability on underwater sound propagation is conducted by interfacing the Chiu-Ehret 3-D acoustic coupled mode (CM) model with a forecasted sound speed field generated by the Harvard Open Ocean Model (HOOM). This research concentrates on the sensitivity of the acoustic wave field to source depth and location with respect to a core ring in the Gulf Stream system for a 50 Hz sound source.

The inclusion of the exact 3-D physics in acoustics modeling requires substantial computer resources. For this reason, it is very desirable to determine when the simpler adiabatic or Nx2-D approximations may be used. To achieve this goal, "exact" 3-D acoustic coupled mode model calculations are compared to results from the adiabatic approximation and the Nx2-D approximation in terms of transmission loss and phases and amplitudes of individual mode modulation envelopes. The results show that the accuracy of the adiabatic and Nx2-D approximations depend strongly on the radial and transverse sound speed gradients along the track and the acoustic quality considered.

Accession For	
NTIS CRA&I	<input checked="" type="checkbox"/>
DTIC TAB	<input type="checkbox"/>
Unannounced	<input type="checkbox"/>
Justification	
By	
Distribution /	
Availability Codes	
Dist	Avail and/or Special
A-1	

TABLE OF CONTENTS

I.	INTRODUCTION	1
	A. BACKGROUND	1
	B. OBJECTIVES	2
II.	THEORY	5
	A. REVIEW OF NORMAL MODE THEORY FOR A HORIZONTALLY STRATIFIED MEDIUM	5
	B. 3-D COUPLED MODE THEORY	7
	C. INTERFACE WITH THE FORECASTED SOUND SPEED FIELD GENERATED BY THE HOOM	11
III.	RESULTS AND ANALYSIS	17
	A. CASE 1: SOURCE IS PLACED OUTSIDE A WARM EDDY	18
	1. Comparison Between the 3-D Adiabatic and 3-D CM Models	18
	a. Source Depth: 1360 m	18
	(1) Amplitude Comparison	18
	(2) Phase Comparison	19
	b. Source Depth: 300 m	20
	(1) Amplitude Comparison	20
	(2) Phase Comparison	20
	c. Transmission Loss Comparison at 300 m and 1360 m Depths	21
	2. Comparison Between the 3-D CM and Nx2-D Models	22
	a. Source Depth: 1360 m	22
	(1) Amplitude Comparison	22
	(2) Phase Comparison	22

b.	Source Depth: 300 m	23
(1)	Amplitude Comparison	23
(2)	Phase Comparison	23
c.	Transmission Loss Comparison at 300 m and 1360 m Depth	23
B.	CASE 2: SOURCE IS PLACED INSIDE A WARM EDDY	24
1.	Comparison Between the 3-D Adiabatic and 3-D CM Models . .	24
a.	Source Depth: 1360 m	24
(1)	Amplitude Comparison	24
(2)	Phase Comparison	25
b.	Source Depth: 300 m	25
(1)	Amplitude Comparison	25
(2)	Phase Comparison	26
c.	Transmission Loss Comparison at 300 m and 1360m	26
2.	Comparison Between the 3-D and Nx2-D CM Models	26
a.	Source Depth: 1360 m	26
(1)	Amplitude Comparison	26
(2)	Phase Comparison	27
b.	Source Depth: 300 m	27
(1)	Amplitude Comparison	27
(2)	Phase Comparison	27
c.	Transmission Loss Comparison at 300 m and 1360 m Depths	27
IV.	CONCLUSIONS AND RECOMMENDATIONS	60
	APPENDIX A - IMPLEMENTATION OF CHIU-EHRET COUPLED MODE MODEL	
	IN A VAX 8250	63
	LIST OF REFERENCES	65
	INITIAL DISTRIBUTION LIST	67

LIST OF FIGURES

2.1	Sound Speed Contours at a depth of 120 m generated by Harvard University Open Ocean Model (Robinson, et al.) for a region in the Gulf Stream current (480 km x 960 km). The location of the domain chosen for the case studies is marked.	13
2.2	Sound Speed Contours (m/s) at a depth of 120 m for a 240 x 510 km ² region containing a warm eddy north of the Gulf Stream system. . . .	14
2.3	CASE 1: Sound source is placed outside the warm eddy region. The acoustic solution domain in a cylindrical coordinate system and six selected paths $\theta = -2^\circ, 6^\circ, 10^\circ, 44^\circ$, and 62° are shown (each tic mark on the pie shaped sector indicates a 2° increment).	15
2.4	CASE 2: Sound source is placed inside the warm eddy region. The acoustic solution domain in a cylindrical coordinate system and three selected paths $\theta = -45^\circ, 0^\circ, 45^\circ$ are shown (each tic mark on the pie shaped sector indicates 2° increment).	16
3.1	Envelope Amplitude of 10 Modes from the 3-D CM Solution Along the Paths $\theta = 2^\circ$ (Figure 3.1a), $\theta = 6^\circ$ (Figure 3.1b), and $\theta = 10^\circ$ (Figure 3.1c). (Source is placed outside a warm eddy at depth = 1360 m) . . .	29
3.2	Envelope Amplitude of 10 Modes from the 3-D CM Solution Along the Paths $\theta = 4^\circ$ (Figure 3.2a), $\theta = 48^\circ$ (Figure 3.2b), and $\theta = 62^\circ$ (Figure 3.2c). (Source is placed outside a warm eddy at depth = 1360 m) . . .	30
3.3	Envelope Amplitude of 10 Modes for the 3-D Adiabatic Approximation Solution Along the Path $\theta = 6^\circ$. (Source is placed outside a warm eddy at depth = 1360 m)	31

3.4	Differences Between the Phases of the 3-D CM and Adiabatic Solutions for Modes 1 (Figure 3.4a) and 18 (Figure 3.4b) at 1° Contour Interval. (Source is placed outside a warm eddy at depth = 1360 m)	32
3.5	Envelope Amplitude of 20 Modes from the 3-D CM Solution Along the Paths $\theta = -2^\circ$ (Figure 3.5a), $\theta = 6^\circ$ (Figure 3.5b), and $\theta = 10^\circ$ (Figure 3.5c). (Source is placed outside a warm eddy at depth = 300 m)	33
3.6	Eigenfunctions Calculated for Modes 1 to 4 at a Horizontal Location .	34
3.7	Eigenfunctions Calculated for Modes 17 to 20 at a Horizontal Location	35
3.8	Envelope Amplitude of 20 Modes in the 3-D CM Solution Along the Paths $\theta = 44^\circ$ (Figure 3.8a), $\theta = 48^\circ$ (Figure 3.8b), and $\theta = 62^\circ$ (Figure 3.8c). (Source is placed outside warm eddy at depth = 300 m)	36
3.9	Differences Between the Phases of Mode 17 in the 3-D CM and Adiabatic Approximation Results Over the Entire Solution Domain at Contour Interval = 4°. (Source is placed outside warm eddy at depth = 300 m)	37
3.10	Differences in Transmission Loss Between the 3-D CM and Adiabatic Results at 300 m depth (Figure 3.10a) and 1360 m depth (Figure 3.10b) along the Path $\theta = 6^\circ$. (Source is placed outside warm eddy for depths of 300 m (Figure 3.6a) and 1360 m (Figure 3.6b))	38
3.11	Differences in Transmission Loss Between the 3-D CM and Adiabatic Results at 300 m depth (Figure 3.11a) and 1360 m depth (Figure 3.11b) along the Path $\theta = 48^\circ$. (Source is placed outside of warm eddy for depths of 300 m (Figure 3.11a) and 1360 m (Figure 3.11b))	39
3.12	Differences in Transmission Loss Between the 3-D CM and Adiabatic Results at 300 m depth (Figure 3.12a) and 1360 m depth (Figure 3.12b) along the Path $\theta = 62^\circ$. (Source is placed outside of warm eddy for depths of 300 m (Figure 3.12a) and 1360 m (Figure 3.12b))	40

3.13 Differences Between the Amplitudes of the 3-D CM and Nx2-D Solutions for Modes 1 (Figure 3.13a) and Mode 17 (Figure 3.13b) at Contour Interval = 1 x 1000. (Source is placed outside warm eddy at depth = 1360 m)	41
3.14 Differences Between the Phases of the 3-D CM and Nx2-D Solutions for Modes 1 (Figure 3.14a) and 17 (Figure 3.14b) at Contour Interval = 1°. (Source is placed outside warm eddy at depth = 1360 m)	42
3.15 Difference Between the Amplitudes of the 3-D and Nx2-D Solutions for Modes 1 (Figure 3.15a) and 17 (Figure 3.15b). (Source is placed outside a warm eddy at depth = 300 m)	43
3.16 Differences Between the Phases of Mode 17 in the 3-D CM and Nx2-D Solutions Over the Entire Solution Domain at Contour Interval = 1°. (Source is placed outside warm eddy at depth = 300 m)	44
3.17 Differences in Transmission Loss Between the 3-D CM and Nx2-D Results at 300 m Depth (Figure 3.17a) and 1360 m depth (Figure 3.17b) along the Path $\theta = 6^\circ$. (Source is placed inside warm eddy for depths of 300 m (Figure 3.17a) and 1360 m (Figure 3.17b))	45
3.18 Differences in Transmission Loss Between the 3-D CM and Nx2-D Results at 300 m Depth (Figure 3.18a) and 1360 m depth (Figure 3.18b) along the Path $\theta = 48^\circ$. (Source is placed inside warm eddy for depths of 300 m (Figure 3.18a) and 1360 m (Figure 3.18b))	46
3.19 Differences in Transmission Loss Between the 3-D CM and Nx2-D Results at 300 m Depth (Figure 3.19a) and 1360 m depth (Figure 3.19b) along the Path $\theta = 62^\circ$. (Source is placed inside warm eddy for depths of 300 m (Figure 3.19a) and 1360 m (Figure 3.19b))	47

3.20	Envelope Amplitudes of 10 of the Modes in the 3-D CM Solution Along the Paths $\theta = -45^\circ$ (Figure 3.20a) and $\theta = 1^\circ$ (Figure 3.20b). (Source is placed inside warm eddy at depth = 1360 m)	48
3.21	Differences Between the Envelope Amplitudes of the 3-D CM and Adiabatic Solutions for Mode 1 at Contour Interval = 1 (Figure 3.21a) and Mode 17 at Contour Interval = 2 (Figure 3.21b). (Source is placed inside warm eddy at depth = 1360 m)	49
3.22	Differences Between the Phases of the 3-D CM and Adiabatic Approximation for Mode 1 at Contour Interval = 1° (Figure 3.22a) and Mode 17 at Contour Interval = 4° (Figure 3.22b). (Source is placed inside warm eddy at depth = 1360 m)	50
3.23	Envelopes Amplitudes of 10 of the Modes in the 3-D CM Solution Along the Paths $\theta = -45^\circ$ (Figure 3.23a) and $\theta = 1^\circ$ (Figure 3.23b). (Source is placed inside warm eddy at depth = 300 m)	51
3.24	Differences Between the Envelope Amplitudes of Modes 17 in the 3-D CM and Adiabatic Approximation over the Entire Solution Domain at Contour Interval = 4. (Source is placed inside warm eddy at depth = 300 m)	52
3.25	Differences Between the Phases of Mode 17 in the 3-D CM and Adiabatic Results over the Entire Solution Domain at Contour Interval = 10° . (Source is placed inside the warm eddy at depth = 300 m)	53
3.26	Differences in Transmission Loss Between the 3-D CM and Adiabatic Approximation Results at 300 m depth (Figure 3.26a) and 1360 m depth (Figure 3.26b) along the Path $\theta = -45^\circ$. (Source is placed inside warm eddy for depths of 300 m (Figure 3.26a) and 1360 m (Figure 3.26b)) . .	54

3.27	Differences in Transmission Loss Between the 3-D CM and Adiabatic Approximation Results at 300 m depth (Figure 3.27a) and 1360 m depth (Figure 3.27b) along the Path $\theta = 1^\circ$. (Source is placed inside warm eddy for depths of 300 m (Figure 3.27a) and 1360 m (Figure 3.27b))	55
3.28	Differences Between the Phases of the 3-D CM and Nx2-D Solutions for Mode 1 (Figure 3.28a) and Mode 17 (Figure 3.28b). Contour Interval for both Graphs = 1° . (Source is inside warm eddy at depth = 1360 m)	56
3.29	Differences Between the Phases of Mode 17 in the 3-D CM and Nx2-D Solutions at Contour Interval = 1° . (Source is placed inside warm eddy at depth = 300 m)	57
3.30	Differences in Transmission Loss Between the 3-D CM and Nx2-D Solutions at 300 m Depth (Figure 3.30a) and 1360 m depth (Figure 3.30b) along the Path $\theta = -45^\circ$. (Source is placed inside warm eddy for depths of 300 m (Figure 3.30a) and 1360 m (Figure 3.30b))	58
3.31	Differences in Transmission Loss Between the 3-D and Nx2-D Solutions at 300 m depth (Figure 3.31a) and 1360 m depth (Figure 3.31b) along the Path $\theta = 1^\circ$. (Source is placed inside warm eddy for depths of 300 m (Figure 3.31a) and 1360 m (Figure 3.31b))	59

I. INTRODUCTION

A. BACKGROUND

The ocean environment as a sound transmitting medium varies both temporally and spatially due to the presence of mesoscale features such as fronts, currents, eddies and internal waves. Our increasing knowledge of the complexity of the structure and dynamics of the world's oceans have led to a broad range of studies on oceanographic influences on underwater acoustics. Numerous works have been published following the pioneering work of Pekeris [Ref. 1], who first illuminated the complexities of shallow water acoustics due to interaction with a penetrable bottom. The basic technique used in Pekeris' work was the method of normal modes in which the acoustic field in the ocean is expressed as a sum of modes propagating independently of each other. Since then, the normal mode theory rapidly became a valuable tool for calculating acoustic propagation. However, most of the studies were confined to cases of vertical variations only. In such stratified media, the velocity profiles and boundaries are independent of range and thus give an exact separation of the wave equation in the radial and vertical directions. Unfortunately, horizontal stratification of the acoustic media is a condition that rarely occurs in the real world. Mesoscale variability in the world's oceans imposes a need for a fully 3-D acoustic propagation model

In 1965, Pierce [Ref. 2] and later Milder [Ref. 3] extended the method of normal modes by deriving a set of coupled mode equations to investigate acoustic propagation for a gradually range-dependent ocean environment known as an "almost-stratified medium." When sound propagates in medium that has both vertical and horizontal variations, the normal modes are coupled and interact continuously. Mathematically,

this means that the equations governing the amplitudes of the modes have to satisfy a coupled set of differential equations describing the exchange of energy between the normal modes. These equations are very difficult to solve when a large number of modes are involved. To avoid this problem, Pierce and Milder employed coupled mode theory in an approximate fashion by performing an “adiabatic” separation of the depth and range coordinates. The principal assumption in adiabatic theory is the neglect of mode-mode coupling based on the idea that as the modes propagate, they progressively adapt to a slowly changing environment. In other words, in the adiabatic approximation the amount of energy initially associated with a mode remains with that modes since energy exchange between modes has been neglected. Detailed discussion of this approximation’s limitations may be found in the work of Desaubies, et al. [Ref. 4].

Extensive research on sound propagation in a range variable environment using ray theory methods [Refs. 5, 6] and parabolic equation methods [Refs. 7-12] have been widely used within the underwater acoustics modeling community. This thesis however uses the 3-D coupled normal mode (CM) model developed by Chiu and Ehret [Ref. 13] to examine the complexity of acoustic-oceanographic interactions. An interface of this 3-D acoustic model with a predicted sound speed field generated by the Harvard Open Ocean Model (HOOM) [Ref. 14] has provided this opportunity to examine the 3-D environmental effects on sound propagation.

B. OBJECTIVES

This thesis has two objectives:

1. Investigate the 3-D environmental effects on low frequency sound transmission. Specifically, this thesis examines the effects of horizontal refraction and mode-mode interaction in the presence of a warm core ring. This warm eddy is located north of the Gulf Stream system.

2. Quantify the accuracy of the "approximate" 3-D adiabatic and Nx2-D coupled mode solutions by comparing them to the "exact" 3-D coupled mode model solutions at two different source/receiver locations with respect to the warm eddy (inner and outer) at two different depths (300 m and 1360 m). The acoustic quantities compared include mode amplitude, mode phase and transmission loss.

The above objectives were accomplished by first running the 3-D acoustic CM model on the VAX 8250 for a 50 Hz sound source placed at the sound channel depth (1360 m) outside of the warm eddy region. The implementation of the acoustic CM model on the VAX mini-computers is discussed in Appendix A. The 3-D adiabatic approximation and the Nx2-D coupled mode models were then run using the same geometric and acoustic parameters. The results from these three runs were compared and discussed to determine the validity of the "approximate" models. The process was then repeated for subsequent cases where the source was moved to the center of the eddy and later to a shallow depth of 300 m.

The computer implementation of the CM algorithm required large amounts of central memory and computer time. The other two "approximate" model algorithms required much less; for the adiabatic approach, computation time was reduced by almost 90%, while the Nx2-D approach was reduced by as much as 50%. Therefore, if the physics may be approximated, the usefulness of the adiabatic and Nx2-D approximations is obvious. The adiabatic model and the Nx2-D model also require significantly less memory storage.

The outline for this thesis is as follows:

- Chapter II contains the mathematical formalism of coupled mode theory as originally proposed by Pierce and later applied in the CM numerical acoustic model.

A discussion of the interfacing procedure of the CM model with the forecasted sound speed field generated by the HOOM is also included.

- Chapter III details the results of the full 3-D acoustic CM solutions and the comparison to the Nx2-D and adiabatic methods. The compared acoustic quantities include mode amplitude, mode phase, and transmission loss. Two test cases are investigated. Case 1 places the source outside of the warm eddy and Case 2 places it inside the core. Comparison and discussion on the propagation in and out of the eddy are made for two different source depths (1360 m, 300 m).
- Chapter IV summarizes the work completed in the thesis, draws conclusions, and suggests recommendations for possible future studies in this endeavor.

II. THEORY

In this chapter, the mathematical formalism of coupled mode theory is presented. First, normal mode theory for a horizontally stratified medium will be reviewed. Next, the extension of normal modes to sound propagation in media containing horizontal variations as well as vertical variations, known as coupled mode theory, will be formulated and discussed.

A. REVIEW OF NORMAL MODE THEORY FOR A HORIZONTALLY STRATIFIED MEDIUM

The essence of ocean acoustic theory is contained in this second order wave equation:

$$\nabla^2 \Phi = \frac{1}{c^2} \frac{\partial^2 \Phi}{\partial t^2} \quad (2.1)$$

where Φ is the acoustic velocity potential or pressure perturbation, c is the sound speed which may vary in the x, y, z coordinates, and ∇^2 is the three dimensional Laplacian operator.

The three mathematical approaches used to solve the wave equation are ray theory approximation, parabolic equation approximation theory, and normal mode theory. This study focuses on the normal mode theory approach.

Normal modes constitute an "exact" solution to the wave equation providing that the boundaries are flat. In normal mode theory, sound propagation is described in terms of characteristic vertical functions called normal modes. Each mode represents a vertical standing wave traveling outward from the source with an amplitude that is a function of radial and transverse variability. The propagating normal modes are combined additively to represent the ocean acoustic field.

The method of normal modes was originally applied by Pekeris [Ref. 1] to study long-range sound propagation. However, this method was confined to the case of stratified media, with the sound speed profiles and boundaries *independent* of range. This neglect of the range variability makes it possible to illustrate many fundamental wave properties by means of simple equations and solutions. When cylindrical geometry is used with the z -axis normal to the ocean surface and pointing down, the wave equation can simply be reduced by separation of variables. This exact separation leads to a system of two linear differential equations, one for depth dependence and the other for range dependence. Specifically, the time independent Helmholtz equation for the acoustic velocity potential $\Phi(r, z)$ to be solved is:

$$\nabla^2 \Phi(r, z) + k^2(z) \Phi(r, z) = -4\pi \delta(r, z - z_0) \quad (2.2)$$

where r is the range from the source, z is the depth, and k is the wave number defined as:

$$k \equiv \frac{\omega}{c(z)} \quad (2.3)$$

for a unit point source of harmonic frequency ω located $z = z_0$, $r = 0$. By assumption, k is taken to be range-independent and depends on a single sound speed profile $c(z)$. Equation (2.2) may be expressed in terms of products of radial and depth functions, i.e.,

$$\Phi(r, z) = \sum R_n(r) Z_n(z) \quad (2.4)$$

Because the horizontal structure of the medium (represented by R_n) is assumed to be invariant, the range equations which govern the evolution of each of the modes are not coupled, i.e., the normal modes propagate independently of each other. The bulk of the remaining problems centers around the evaluation of the depth functions, i.e., the normal modes. The particular form of the solution for Z_n depends upon the functional description of the sound speed profiles and the boundary constraints.

B. 3-D COUPLED MODE THEORY

The description of the open ocean as a horizontally stratified fluid is only an approximation to the actual physical situation. The sound field in the ocean is strongly affected by the variation of the temperature and salinity with horizontal distance as well as depth. Consequently, the modes which represent the acoustic field in such a variable ocean do not propagate independently (as in the case of a perfectly stratified medium) of each other; they are coupled and interact continuously [Ref. 13]. In other words, when *range dependence* of the medium is present, an exchange of energy between modes occurs and the partitioning of energy between modes changes with range from the source.

In 1965, Pierce introduced the theory of acoustic propagation via coupled normal modes for guided wave propagation in a medium that varied slowly with range in addition to varying with depth [Ref. 2]. The mathematical formalism of this coupled mode theory forms the basis of a 3-D acoustic CM model developed by Chiu and Ehret [Ref. 13], used in this study.

The reduced wave equation for the velocity potential in a medium with depth, range and azimuth dependence due to a point harmonic source is:

$$\left[\nabla^2 + k^2(\vec{x}) \right] \Phi(\vec{x}) = -4\pi\delta(\vec{x} - \vec{x}_0) \quad (2.5)$$

In Equation 2.5, cylindrical coordinates are used and $\vec{x} = (r, \theta, z)$ where r is the range, θ is the azimuth angle measured positive counterclockwise, and z is the depth. The extension of the method of normal modes now treats the sound speed as a function of 3-D space, $c = c(\vec{x})$, to account for the sound speed fluctuations caused by fronts and eddies. The above equation describes a field with a point source located at \vec{x}_0 and oscillating at an acoustic frequency of ω . Boundary conditions currently used in the CM model are a pressure release flat surface and a hard flat bottom.

The method employed here to obtain the solution to Equation 2.5 is one used by Chiu and Ehret. Analogous to earlier mode theory, coupled mode theory expresses the solution as a linear combination of the local normal modes Z_n

$$\Phi = \frac{1}{\sqrt{r}} \sum_n P_n(r, \theta) Z_n(z; r, \theta) \quad (2.6)$$

where the normal modes satisfy:

- The depth equation

$$\left[\frac{\partial^2}{\partial z^2} + (k^2 - k_n^2) \right] Z_n = 0 \quad (2.7)$$

- Surface and bottom boundary conditions

$$\begin{aligned} Z_n(0; r, \theta) &= 0 \\ \frac{\partial}{\partial z} Z_n(-H; r, \theta) &= 0 \end{aligned} \quad (2.8)$$

- Orthonormality condition

$$\int_{-H}^0 \rho Z_n Z_m dz = \delta_{m,n} \quad (2.9)$$

where ρ is the density, H is the ocean depth, k is the total wave number and k_n is the horizontal wave number.

The coupled mode equations governing the mode amplitude functions, P_n , can be obtained by substituting Equation 2.6 into the wave Equation 2.5 and then applying the conditions given in Equations 2.7, 2.8, and 2.9 [Ref. 13].

For the far field where $kr \gg 1$, the coupled mode equations are:

$$\left(\frac{\partial^2}{\partial r^2} + k_n^2 + \frac{1}{r^2} \frac{\partial^2}{\partial \theta^2} \right) P_n = - \sum_m \left[\left(\gamma_{mn} \frac{\partial}{\partial r} + \beta_{mn} \frac{1}{r} \frac{\partial}{\partial \theta} \right) + B_{mn} \right] P_m \quad (2.10)$$

where γ_{mn} and β_{mn} are the coupling coefficients defined as

$$\begin{aligned}\gamma_{mn}\hat{r} + \beta_{mn}\hat{\theta} &= 2 \int \rho Z_n \nabla Z_m dz \\ &= \begin{cases} \frac{4}{k_n^2 - k_m^2} \int \rho (k \nabla k) Z_m Z_n dz & m \neq n \\ 0 & m = n \end{cases} \\ B_{mn} &= \int \rho Z_n \nabla^2 Z_m dz \\ &= \frac{1}{2} \left\{ \frac{\partial}{\partial r} \gamma_{mn} + \frac{1}{r} \frac{\partial}{\partial \theta} \beta_{mn} + \frac{1}{2} \sum_l (\gamma_{ln} \gamma_{ml} + \beta_{ln} \beta_{ml}) \right\}\end{aligned}$$

where ∇ is now a two-dimensional horizontal gradient operator.

The above coupling coefficients express the rates of interchange of acoustic energy between modes m and n as the signal propagates outward from the source. In the stratified case where there is no horizontal sound speed variation, the acoustic energy initially associated with a mode remains with that mode, the coupling terms in Equation 2.10 vanish, and each mode amplitude function P_n remains constant with range. The mode amplitude P_n is approximately constant for cases where there is sufficiently slow range variation of the medium. In such cases, the adiabatic approximation is applicable. Such approximation is based on the assumption that the effects of mode-mode coupling become small in a slowly changing environment and therefore may be neglected. However, under more variable oceanic conditions due to ocean fronts, meanders, and eddies, appreciable horizontal sound speed variations do exist and cause a transfer of energy between modes. The mode amplitude P_n is no longer constant but varies in both the radial and azimuthal directions with periods equal to the mode interference distances $2\pi/(k_n - k_m)$ and the ocean perturbation length scales, respectively [Ref. 13].

There is an obvious computational advantage to assuming a near adiabatic solution modulated by a slowly varying complex envelopes and solving for the envelopes rather than P_n 's [Ref. 13]. By solving for these modulation envelopes, a much larger

integration step size, a fraction of the characteristic length of ocean perturbations, can be used for the computation [Ref. 13]. To implement this assumption and take the rapid variations out of P_n , the following decomposition is made

$$P_n = U_n(r, \theta) e^{i\phi_n(r, \theta)} \quad (2.11)$$

where

$$\phi_n = \int_0^r k_n(r, \theta) dr$$

The governing equations for the slowly varying envelopes U_n 's can be obtained by substituting Equation 2.11 into Equation 2.10 [Ref. 13]:

$$D_n \left(\frac{\partial^2}{\partial r^2} + \frac{1}{r^2} \frac{\partial^2}{\partial \theta^2} \right) U_n + \left(\frac{\partial}{\partial r} + E_n \right) U_n + F_n \frac{1}{r} \frac{\partial}{\partial \theta} U_n = \sum_m \tilde{G}_{mn} \cdot \nabla U_m + \sum_m H_{mn} U_m \quad (2.12)$$

where

$$\begin{aligned} D_n &= \frac{-i}{2k_n} \\ E_n &= \frac{1}{2k_n} \left[\frac{\partial}{\partial r} k_n + \frac{1}{r^2} \frac{\partial^2}{\partial \theta^2} \phi_n + \frac{i}{r^2} \left(\frac{\partial}{\partial \theta} \phi_n \right)^2 \right] \\ F_n &= \frac{1}{k_n r} \left(\frac{\partial}{\partial \theta} \phi_n \right) \\ \tilde{G}_{mn} &= \frac{i}{2k_n} \left[\gamma_{mn} \hat{r} + \beta_{mn} \hat{\theta} \right] e^{i(\phi_m - \phi_n)} \\ H_{mn} &= \begin{cases} \frac{-1}{2k_n} \left[\gamma_{mn} k_m + \frac{\beta_{mn}}{r} \frac{\partial}{\partial \theta} \phi_m - i B_{mn} \right] e^{i(\phi_m - \phi_n)} & m \neq n \\ \frac{i}{2k_n} B_{nn} & m = n \end{cases} \end{aligned}$$

To obtain the coupled mode solution, Equations 2.7, 2.8, 2.9 and 2.12 need to be solved.

The CM model numerically integrates the differential equations governing the complex envelopes in the radial direction and iterates in the azimuthal direction to

construct a 3-D solution in a cylindrical coordinate system. The slowly varying envelopes can be computed accurately using a step size an order of magnitude longer than the acoustic wavelength. Details of the implementation of the CM model on a VAX 8250 are discussed in Appendix A.

C. INTERFACE WITH THE FORECASTED SOUND SPEED FIELD GENERATED BY THE HOOM

To investigate the effects of the transverse and radial sound speed gradients on sound propagation, an interface of the 3-D CM model with the HOOM is performed.

The HOOM is a quasigeostrophic, open boundary, ocean model developed by Robinson, et al. [Ref. 14] to forecast the ocean fields in the Gulf Stream region. This model contains six vertical levels (at 100, 300, 700, 1100, 2200, and 3900 m, respectively), and has a horizontal resolution of 15 km. Due to the widely spaced vertical and horizontal computational grid points found in the ocean model output, two tasks are required to accomplish the interfacing procedures. The first task is the interpolation of continuous sound speed profiles in the vertical in order to realistically compute the acoustic normal modes, acoustic mode wavenumbers, and coupling coefficients. The second task is the construction of continuous functions of acoustic mode wavenumbers and coupling coefficients along radial paths. These two tasks were accomplished by fitting cubic and bi-cubic spline surfaces to values existing at grid points [Ref. 13]. For this study, 100 data points are interpolated from the modelled vertical six point sound speed profile to get a vertical resolution of 40 m necessary for the calculation of normal modes over the 4 km ocean depth.

The sound speed contours associated with this ocean model at a depth of 120 m are illustrated in Figure 2.1. This figure shows the Gulf Stream front, located almost parallel to the x-axis, a meander, a warm eddy to the north, and a cold eddy to the

south. Of particular interest are the strong sound speed gradients existing across the Gulf Stream front and at the perimeter of the eddies and meander. The location of the domain ($240 \times 510 \text{ km}^2$) chosen for the two case studies is marked.

Figure 2.2 is an enlargement of the study area to illustrate the appreciably strong sound speed gradients (approximately $.8 \text{ m/s}$ in 5 km) across a small section of the Gulf Stream and the entire warm eddy region.

To examine the 3-D environmental effects on sound propagation through the warm eddy, two case studies are performed.

In Case 1, a 50 Hz sound source is placed outside the core ring. The acoustic solution domain in a cylindrical coordinate system is marked in Figure 2.3. The pie shaped sector is bounded by the -2° and 72° tracks. It is important to note that significant transverse sound speed gradients are found in this sector.

In Case 2, a 50 Hz sound source is placed within the warm eddy. The acoustic solution domain for this case is displayed in Figure 2.4. This pie shaped sector is subtended by -45° and 45° allowing a complete examination of the inner part of the eddy and its effects on sound propagation. The interesting features observed in this case are the large radial sound speed gradients.

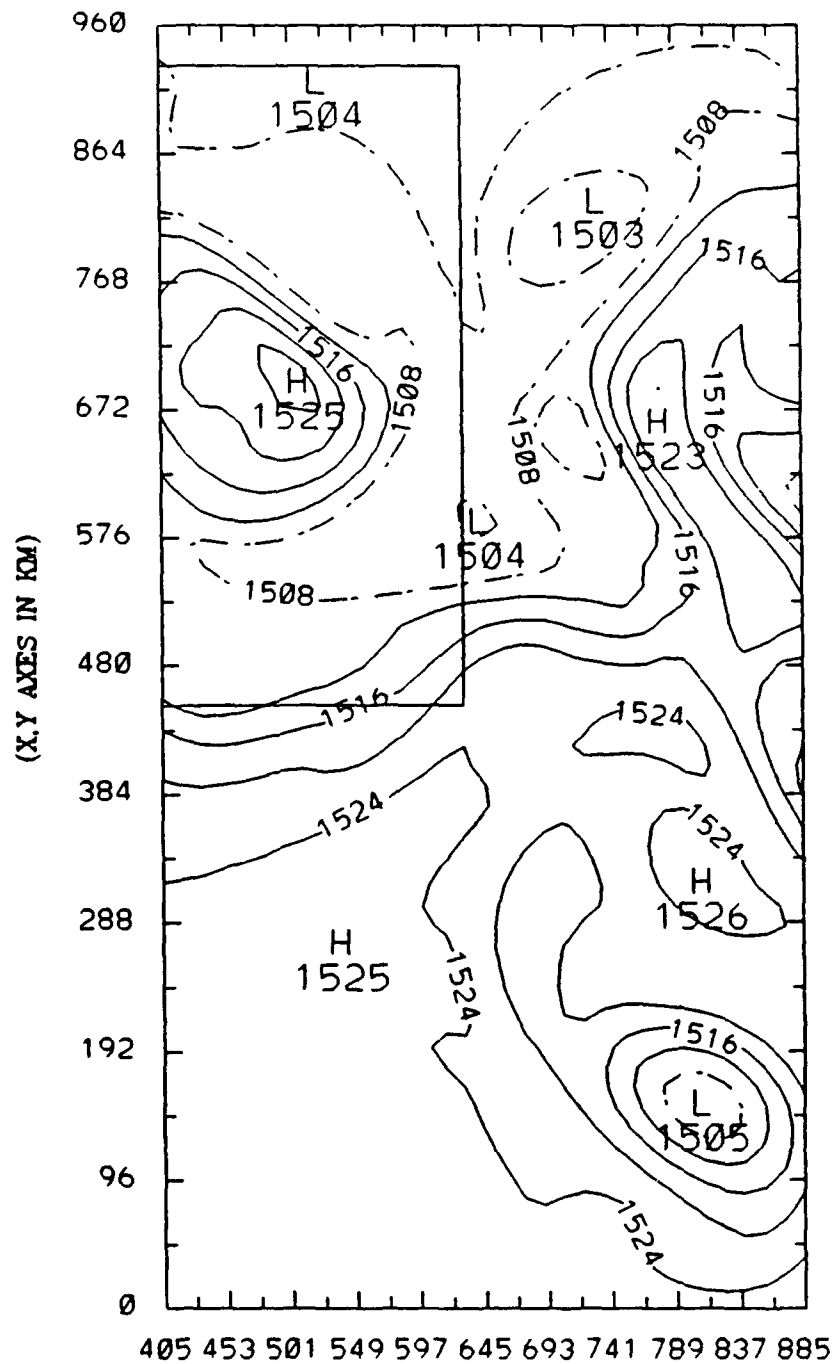


Figure 2.1: Sound Speed Contours at a depth of 120 m generated by Harvard University Open Ocean Model (Robinson, et al.) for a region in the Gulf Stream current (480 km x 960 km). The location of the domain chosen for the case studies is marked.

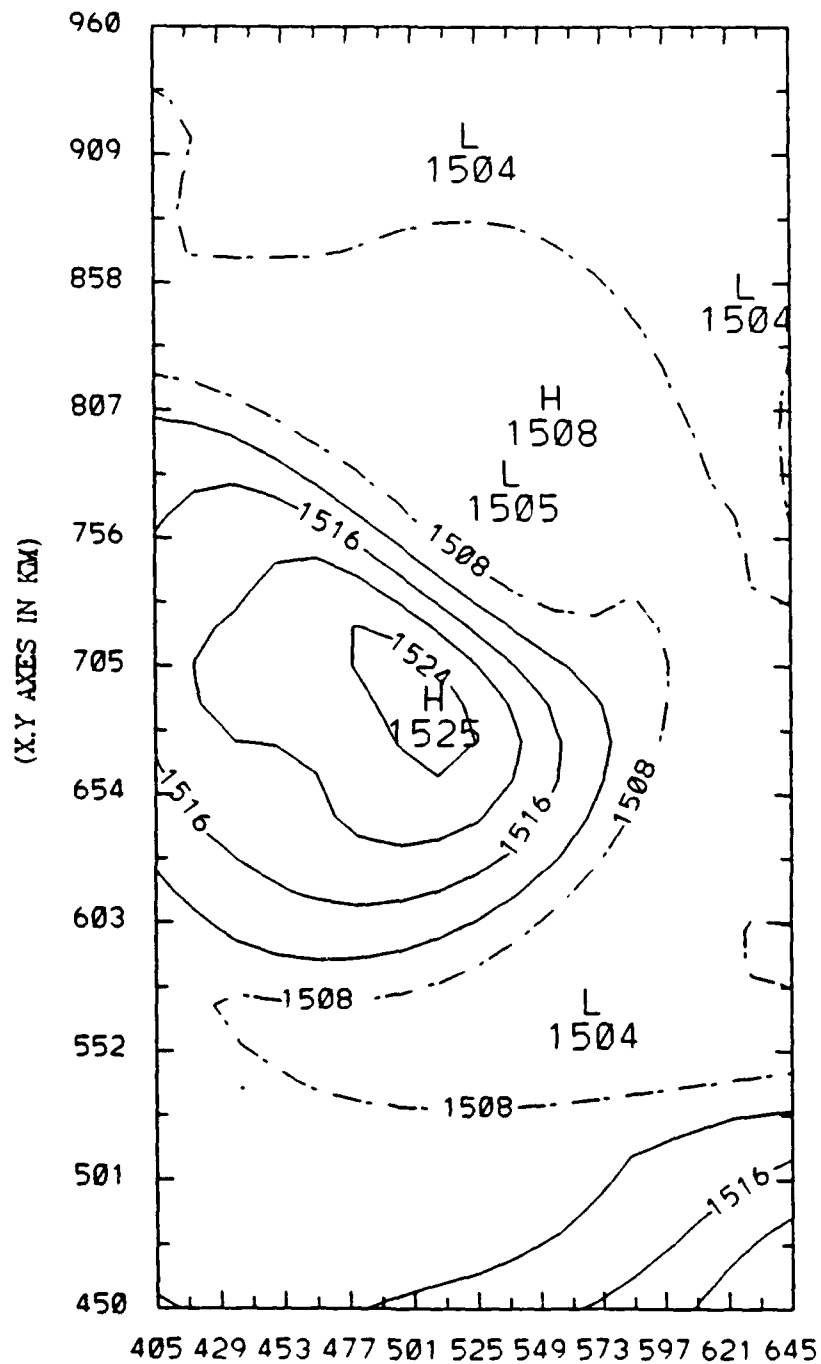


Figure 2.2: Sound Speed Contours (m/s) at a depth of 120 m for a 240 x 510 km² region containing a warm eddy north of the Gulf Stream system.

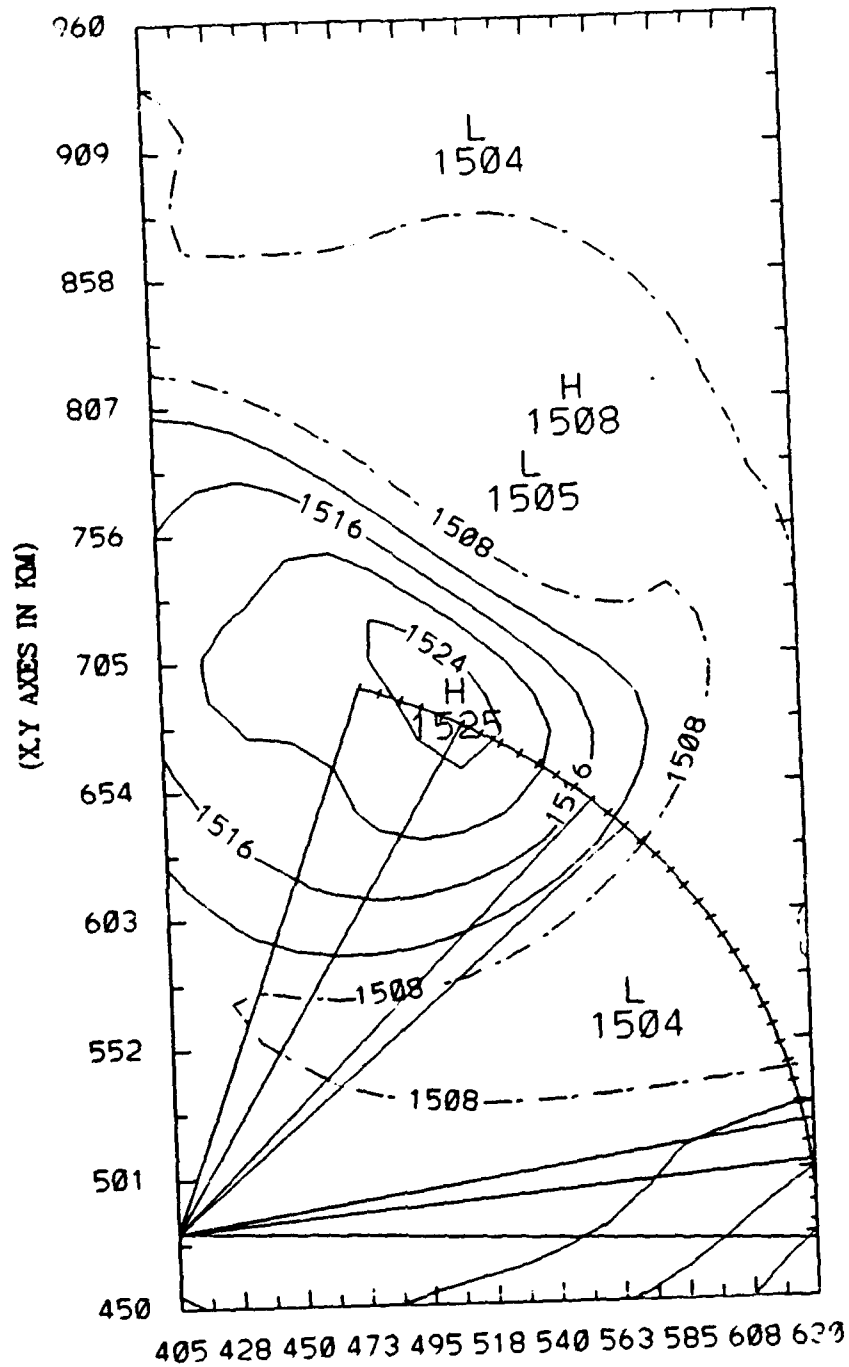


Figure 2.3: CASE 1: Sound source is placed outside the warm eddy region. The acoustic solution domain in a cylindrical coordinate system and six selected paths $\theta = -2^\circ, 6^\circ, 10^\circ, 44^\circ$, and 62° are shown (each tic mark on the pie shaped sector indicates a 2° increment).

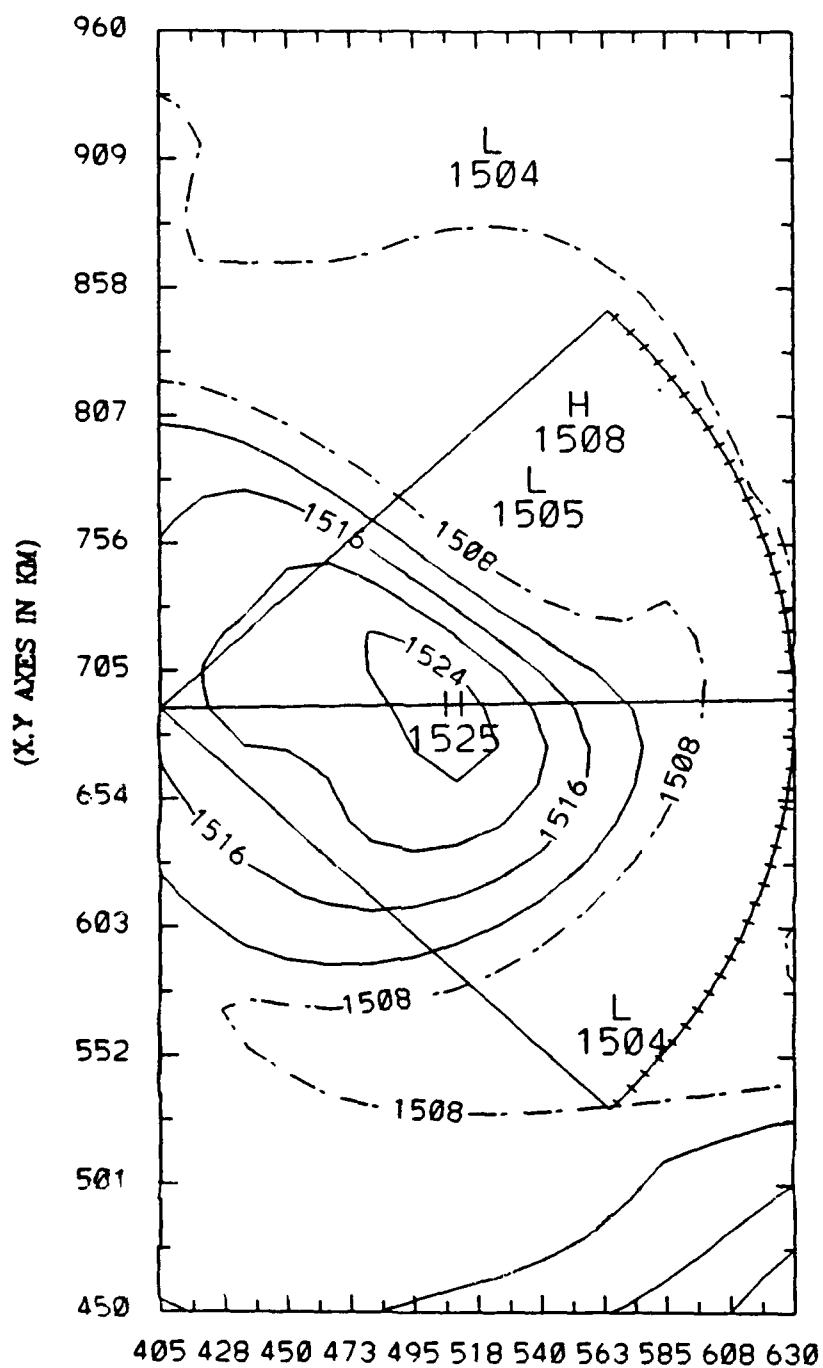


Figure 2.4: CASE 2: Sound source is placed inside the warm eddy region. The acoustic solution domain in a cylindrical coordinate system and three selected paths $\theta = -45^\circ, 0^\circ, 45^\circ$ are shown (each tic mark on the pie shaped sector indicates 2° increment).

III. RESULTS AND ANALYSIS

Three acoustic models are used to investigate the effects on sound propagation of various sound speed gradients found inside and outside of the observed warm eddy. They are: 3-D CM model, 3-D adiabatic approximation model, and Nx2-D approximation model. The acoustic field computed using the adiabatic approximation method neglects all mode coupling terms, reducing computer time by as much as 90%. With the Nx2-D approach, azimuthal homogeneity is assumed and thus all the terms involving derivatives with respect to θ are dropped. The computer time of the Nx2-D algorithm is faster than the 3-D algorithm by about 50%. The acoustic parameters used for the model runs are:

- Acoustic Frequency: 50 Hz
- Source Depth: 1350 m (sound channel axis) and 300 m
- Solution Domains:
 - Case 1: Propagating source is outside of warm eddy
 $r < 220 \text{ km}$ and $-2^\circ < \theta < 72^\circ$
 - Case 2: Propagating source is inside of warm eddy
 $r < 220 \text{ km}$ and $-45^\circ < \theta < 45^\circ$
- Ocean Depth: 4 km
- Radial integration step size: 5 km
- Angular resolution: 2°

Since the warm eddy region contains strong sound speed gradients, it is ideally suited to demonstrate the three dimensional acoustic effects over a 220 km range with various source/receiver locations. This study deals with two horizontal and two vertical source/receiver configurations.

The purpose of these runs is to compare the approximate models to the accuracy of the "exact" CM model in terms of phases and amplitudes of the individual modes, and transmission loss. The comparisons establish the validity of the two approximate solutions for modeling sound transmission in the warm eddy region.

A. CASE 1: SOURCE IS PLACED OUTSIDE A WARM EDDY

1. Comparison Between the 3-D Adiabatic and 3-D CM Models

a. Source Depth: 1360 m

(1) Amplitude Comparison

To investigate the effects of the strong transverse sound speed gradients on sound propagation originating outside of the warm eddy, acoustic quantities along six radial paths are examined (See Figure 2.3). These six paths are along -2° , 6° , 10° , 44° , 48° , and 62° . The envelope amplitudes of 10 of the modes from the 3-D CM solutions along these paths are then plotted to examine the mode coupling effects due to the highly variable environment.

In Figure 3.1a, along the path $0 = -2^\circ$, the envelope amplitudes indicate continuous interactions between the 1st and 2nd modes, the 6th and 7th modes, the 13th and 14th modes, and the 18th and 19th modes. These neighboring modes are tightly coupled, indicating an exchange of energy between the modes. As energy increases in one of the modes, the energy in the adjacent mode decreases. This coupling effect is stronger at higher modes. The envelope amplitudes of 10 modes in the 3-D CM solutions calculated along the 6° (Figure 3.1b) and 10° (Figure 3.1c) radial

paths which traverse a small section of the Gulf Stream front (Figure 2.3) also exhibit similar behavior to that along the -2° path. The strongest transverse gradient for these paths is 4 m/s in 23 km. For the paths that intersect the warm core eddy along which the radial sound speed variation is large (averaging 4 m/s per 35 km), mode coupling becomes even more significant. The strong mode-mode interactions for these paths ($\theta = 44^\circ, 48^\circ$, and 62°) are illustrated in Figure 3.2a, b, and c, respectively.

Unlike the 3-D CM solution, the mode amplitudes in the 3-D adiabatic solution are constant in range due to the neglect of mode coupling terms. Figure 3.3 depicts this result for a 6° path. Hence, the difference between the envelope amplitudes of the 3-D adiabatic and CM solutions indicates the inappropriateness of the adiabatic approximation for regions of large radial sound speed gradient.

(2) Phase Comparison

Figures 3.4a and b display the differences between the phases in the 3-D CM and adiabatic solutions for the entire solution domain for modes 1 and 18, respectively. These two modes are representative of the low modes and high modes.

For mode 1, phase errors in the adiabatic approximation are concentrated and accumulated along the small section of the Gulf Stream and edge of the warm ring. In these two locations, radial sound speed gradient is roughly 4 m/s per 20 km (refer to Figure 2.3). The phase errors grow to 16° along the edge of the warm ring and 11° along the small section of the Gulf Stream. As the mode number increases, the phase errors generally decrease. At mode 18, the phase errors decrease to 6° . The largest phase errors are colocated with the regions of high transverse sound speed gradient. However, the phase errors are still small, i.e., the adiabatic phase results are adequate.

b. Source Depth: 300 m

(1) Amplitude Comparison

Figures 3.5a, b, and c display the envelope amplitude of 10 of the modes for the 3-D CM solution with the new source depth at $\theta = -2^\circ$, 6° , and 10° , respectively. The envelope amplitudes of all 20 modes were plotted; however, only mode 9 and higher modes have amplitudes that significantly differ from zero. Such results are to be expected since a shallow source distributes more energy to the higher modes (see Figures 3.6 and 3.7). Coupling between neighboring modes is evident but weak for θ lying between -2° to 10° . These weak interactions for a shallow source imply that the adiabatic approximation is a fairly good assumption in locations where the transverse sound speed gradient is large. However, this is not the case in locations where the radial sound speed gradient is large. This observation is illustrated in Figures 3.8a, b, and c for the envelope amplitudes of 10 modes along $\theta = 44^\circ$, 48° , and 62° , respectively. Significant fluctuations in the amplitudes are detected at $\theta = 62^\circ$ where the path encounters the largest radial change in the sound speed. Stronger mode-mode interactions are observed at very high mode numbers and at longer range.

(2) Phase Comparison

Figure 3.9 displays the differences in phase of mode 17 between the 3-D CM and adiabatic approximation solutions for the entire acoustic domain. Mode 17 is representative of the high modes excited by a shallow source depth. The phase errors in the adiabatic approximation grow to roughly 30° and are largest in the area of large radial sound speed gradients. Thus, for a shallow source and propagation into locations of large radial sound speed gradients, the adiabatic approximation does not accurately predict neither amplitude nor phase of the mode envelopes.

c. Transmission Loss Comparison at 300 m and 1360 m Depths

Figures 3.10, 3.11, and 3.12 display the differences in transmission loss between the 3-D CM and adiabatic solutions at two depths (300 m, 1360 m) along three selected paths at $\theta = 6^\circ$, 48° , and 62° , respectively.

Along the 6° path, the radial sound speed gradient is small and yields generally small transmission loss error for both source depths. For the sound channel axis source (Figure 3.14a), there is a transmission loss of 13 dB at 20 km, a region where the CM amplitudes exhibit strong mode coupling.

At 48° , the path crosses the periphery of the warm eddy (refer to Figure 2.3) containing the transverse and radial sound speed gradients of approximately 4 m/s per 25 km. For a source depth of 300 m (Figure 3.11a), errors of 2 dB are found along this path for ranges of less than 140 km and greater than 170 km. Errors of 5 dB are found between 140 km to 170 km from the source where the acoustic waves start to make contact with the edge of the warm eddy where the largest radial sound speed gradient is found. For a 1360 m source depth (Figure 3.11b), the average errors grow gradually with range.

At 62° , the path goes through the center of the warm eddy where the radial sound speed gradient increases significantly, up to 4 m/s per 12 km (refer to Figure 2.3). Transmission loss errors up to 10 dB are found for the channel axis source (Figure 3.12a), and up to 5 dB for the shallow source (Figure 3.12b).

Based on the above results, transmission loss error is generally smaller for the shallower source. The transmission loss errors grow gradually with increasing radial sound speed gradient for a SOFAR axis source; whereas for the shallow source, transmission loss error remains small until encountering a very large radial sound speed gradient. Similar to the modal amplitude results, transmission loss as predicted using the adiabatic approximation is largely adequate for regions of small radial sound

speed gradient. For significant radial sound speed gradient, accurate transmission loss calculation requires consideration of mode coupling.

2. Comparison Between the 3-D CM and Nx2-D Models

a. Source Depth: 1360 m

(1) Amplitude Comparison

Figures 3.13a and b display the differences between the amplitudes of the 3-D CM and Nx2-D solutions in the entire solution domain for modes 1 and 17, respectively. The envelope amplitudes of these show that the Nx2-D solutions are almost identical to those of the 3-D CM solution. Since the Nx2-D approximation model neglects all azimuthal variations in its calculations, the results obtained imply that mode amplitudes in the studied domain are minimally affected by the transverse (azimuthal) sound speed variations. The Nx2-D model, therefore, gives accurate mode amplitudes everywhere in the acoustic solution domain for Case 1 (source outside eddy).

(2) Phase Comparison

Figures 3.14a and b display the differences between the phases of the 3-D CM and Nx2-D solutions in the entire solution domain for modes 1 and 17, respectively.

At mode 1, the phase errors in the Nx2-D approximation are concentrated and accumulated along the Gulf Stream and edge of the warm ring. By neglecting azimuthal variations in the Nx2-D model, the phase errors can grow up to 15° in locations where large transverse sound speed gradients, 4 m/s per 15 km, are observed. The phase errors decrease as the mode number increases. At mode 17, phase errors are only visible at the edge of the warm ring and fall off to 6° .

b. Source Depth: 300 m

(1) Amplitude Comparison

Figures 3.15a and b display the differences between the amplitudes of the 3-D and Nx2-D CM solutions for a 300 m source depth over the entire solution domain for modes 1 and 17, respectively. Similar to the results obtained for the 1360 m source depth, there is minimal amplitude error in the Nx2-D coupled mode model. Negligible amplitude errors in the Nx2-D were also found in all other modes (Figures not shown here). Thus, it is evident that the Nx2-D approximation gives good amplitude calculations everywhere over the warm eddy region.

(2) Phase Comparison

Figure 3.16 displays the differences between the phases of the 3-D Cm and Nx2-D solutions in the entire solution domain for a high mode. Errors of only 6° are detected at the edge of the warm ring where strong azimuthal sound speed gradients are present (refer to Figure 2.3).

c. Transmission Loss Comparison at 300 m and 1360 m Depth

Figures 3.17, 3.18, and 3.19 display the differences in transmission loss between the 3-D and Nx2-D Cm solutions at two depths (300 m and 1360 m) along paths at $\theta = 6^\circ$, 48° , and 62° , respectively (refer to Figure 2.3). Insignificant errors in the Nx2-D solutions are obtained indicating that the Nx2-D approximation for transmission loss calculations is valid for a deep (as well as shallow), low frequency source transmitting energy through a warm eddy to a range of 225 km. By switching to Nx2-D calculations in this regime, one can greatly reduce computer time.

B. CASE 2: SOURCE IS PLACED INSIDE A WARM EDDY

1. Comparison Between the 3-D Adiabatic and 3-D CM Models

a. Source Depth: 1360 m

To display the effects on sound propagation due to the significant radial sound speed gradients inside the warm eddy, two paths are chosen as shown in Figure 2.4. These paths are at $\theta = -45^\circ$ and $\theta = 1^\circ$, traversing the edge and center of the warm eddy, respectively.

(1) Amplitude Comparison

Figures 3.20a and b display the envelope amplitudes of 10 of the modes in the 3-D CM solutions along the -45° and 1° paths. At the edge of the warm eddy (Figure 3.20b) where the sound speed gradient in the radial direction is initially small, weak coupling of the lower modes is observed. However, as the mode number and range (with increasing radial sound speed gradient) increase, mode-mode interactions become more significant. Recall that the adiabatic solution has constant amplitude.

For the 1° path (Figure 3.20b) where the radial sound speed gradients increase rapidly toward the center, significant amplitude fluctuations and mode-mode interactions are evident, especially at modes 17, 18, 19, and 20. At the center of the eddy, a region of zero sound speed gradient, the amplitude flattens (near 90 km). The significance of mode coupling, particularly for the higher modes is further illustrated in Figures 3.21a and b where the differences between the amplitude of modes 1 and 17 in the 3-D CM and adiabatic mode solutions in the entire solution domain are shown. The results suggest that for source depths at the SOFAR axis, the 3-D adiabatic mode model approximates the sound propagation rather well when the lower modes are excited. However, the adiabatic approximation model is not valid when

the higher modes are excited, particularly in locations where the radial sound speed gradient is large, such as inside a warm eddy.

(2) Phase Comparison

Figures 3.22a and b display the differences between the phases of the 3-D CM and adiabatic approximation solutions in the entire solution domain for modes 1 and 17, respectively. At mode 1, the phase errors are not significant. At mode 17, phase errors grow only to 14° in regions of large radial sound speed gradients (refer to Figure 2.4).

b. Source Depth: 300 m

(1) Amplitude Comparison

Figures 3.23a and b display the envelope amplitudes of 10 of the modes in the 3-D CM solution along the -45° and 1° paths, respectively. As expected, at a shallower source depth, only mode 9 and higher modes are excited. Coupling between neighboring modes is observed for the highest modes especially for mode 20 along the 1° path. At mode 17, the amplitude error in the adiabatic approximation model is significant at the center of the warm eddy, as illustrated in Figure 3.24. It is interesting to compare these results with the results obtained from Case 1 (source outside eddy) to determine the regimes for which mode coupling is significant. For a source depth of 300 m depth, the amplitude fluctuations in Case 1 are smaller even at higher modes (See Figures 3.8a, b, and c). The Case 1, 62° path encounters ever increasing sound speed. Here, for Case 2, the 1° path encounters first an increase in sound speed and then a sharp decrease. The results imply that mode coupling is more significant in Case 2. Thus, the adiabatic mode model should not be used for the paths crossing through the center of the warm eddy where significantly large radial sound speed gradients exist.

(2) Phase Comparison

Figure 3.25 displays the differences between the phases in the 3-D CM and adiabatic approximation solutions in the entire solution domain for mode 17. Significant phase errors are found in regions of large radial sound speed gradient. Errors of up to 70° are detected. The adiabatic approximation degrades substantially in locations where the radial sound speed gradients are significant, such as inside the core rings.

c. Transmission Loss Comparison at 300 m and 1360m

Figures 3.26 and 3.27 display the differences in transmission loss between the 3-D CM and adiabatic mode solutions at depths (300m, 1360 m) along two chosen paths at $\theta = -45^\circ$ and 1° , respectively.

The -45° path is located at the lower bound of the solution domain. Along this path, for the shallow source depth, the transmission loss error is less than 3 dB. At the SOFAR axis (1360 m depth and for a SOFAR axis source), the transmission loss error reaches 10 dB.

For the path that crosses the center of the warm eddy ($\theta = 1^\circ$), transmission loss error is appreciable. At approximately 200 km from the source location, errors of greater than 15 dB are found for both source depths.

2. Comparison Between the 3-D and Nx2-D CM Models

a. Source Depth: 1360 m

(1) Amplitude Comparison

The Nx2-D CM model contains the coupling mechanisms; it was found to give accurate mode amplitudes everywhere in the warm eddy region (Figure not shown here).

(2) Phase Comparison

Figures 3.28a and b display the differences between the phases of the 3-D and Nx2-D models for modes 1 and 17, respectively, in the solution domain. For both modes, the phase errors in the Nx2-D are small. The phase errors obtained in Case 2 (source inside eddy) are even smaller than those detected in Case 1 (source outside eddy). The reason is that in Case 2, the transverse sound speed gradients are much weaker than those found in Case 1. Similar to Case 1, the phase errors decrease as the mode number increases.

b. Source Depth: 300 m

(1) Amplitude Comparison

There is negligible amplitude error in the Nx2-D approximation (Figure not shown here).

(2) Phase Comparison

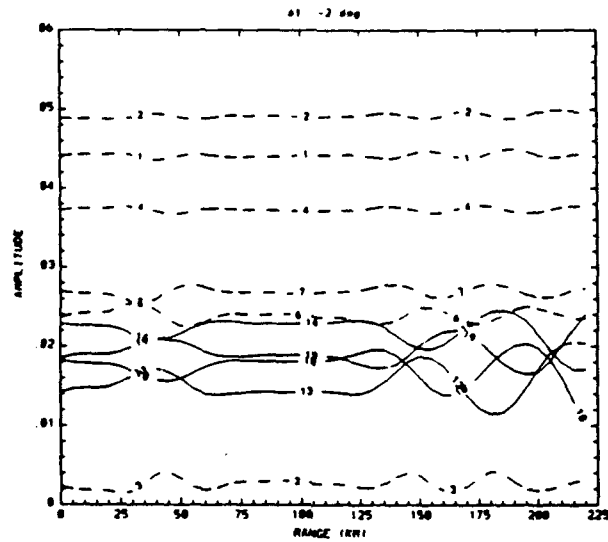
Figure 3.29 displays the differences between the phases of the 3-D and Nx2-D CM solutions over the entire solution domain for a dominant mode. The phase errors in the Nx2-D approximation are quite small for the shallow source.

c. Transmission Loss Comparison at 300 m and 1360 m Depths

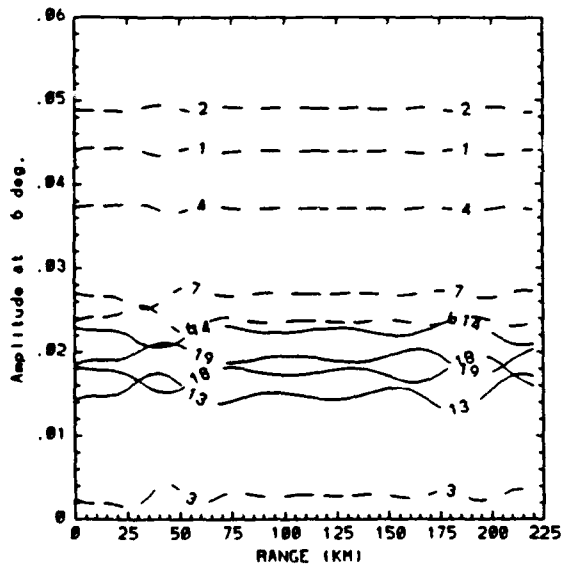
Figures 3.30 and 3.31 display the differences in transmission loss between the 3-D and Nx2-D CM solutions along the paths $\theta = -45^\circ$ and 1° , respectively, (at depths 300 m and 1360 m). For the shallow source, transmission loss difference between 3-D CM and Nx2-D models is negligible (Figures 3.29a and 3.30a). However, transmission loss errors are substantial at the SOFAR axis for a source at the same depth (Figures 29b, 30b). This is due to the fact that low modes are affected more by the transverse sound speed gradient. Both paths have surges of transmission loss at the edge of the eddy or leaving the highest gradient area. The 1° path (passing

through the eddy center) also has a surge near the center where the zero sound speed gradient is followed by a large negative gradient region. Based on the results obtained, the application of Nx2-D approximation is not recommended for a SOFAR axis source when the transverse sound speed gradients are large.

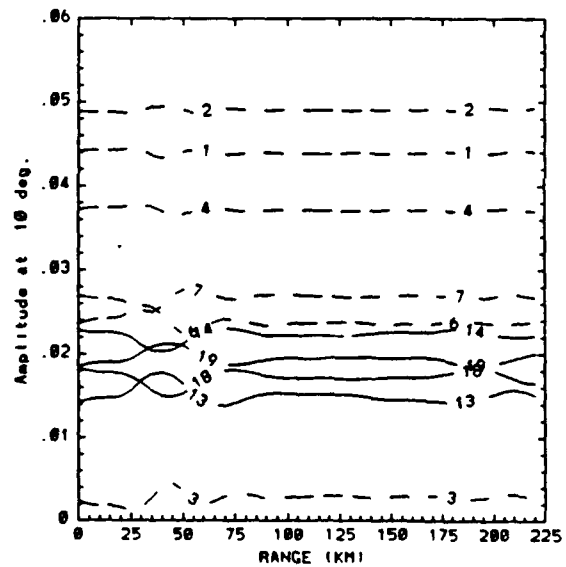
CASE 1
ENVELOPE AMPLITUDE (3-D COUPLED MODE)



a



b



c

Figure 3.1: Envelope Amplitude of 10 Modes from the 3-D CM Solution Along the Paths $\theta = 2^\circ$ (Figure 3.1a), $\theta = 6^\circ$ (Figure 3.1b), and $\theta = 10^\circ$ (Figure 3.1c). (Source is placed outside a warm eddy at depth = 1360 m)

CASE 1
ENVELOPE AMPLITUDE (3-D COUPLED MODE)

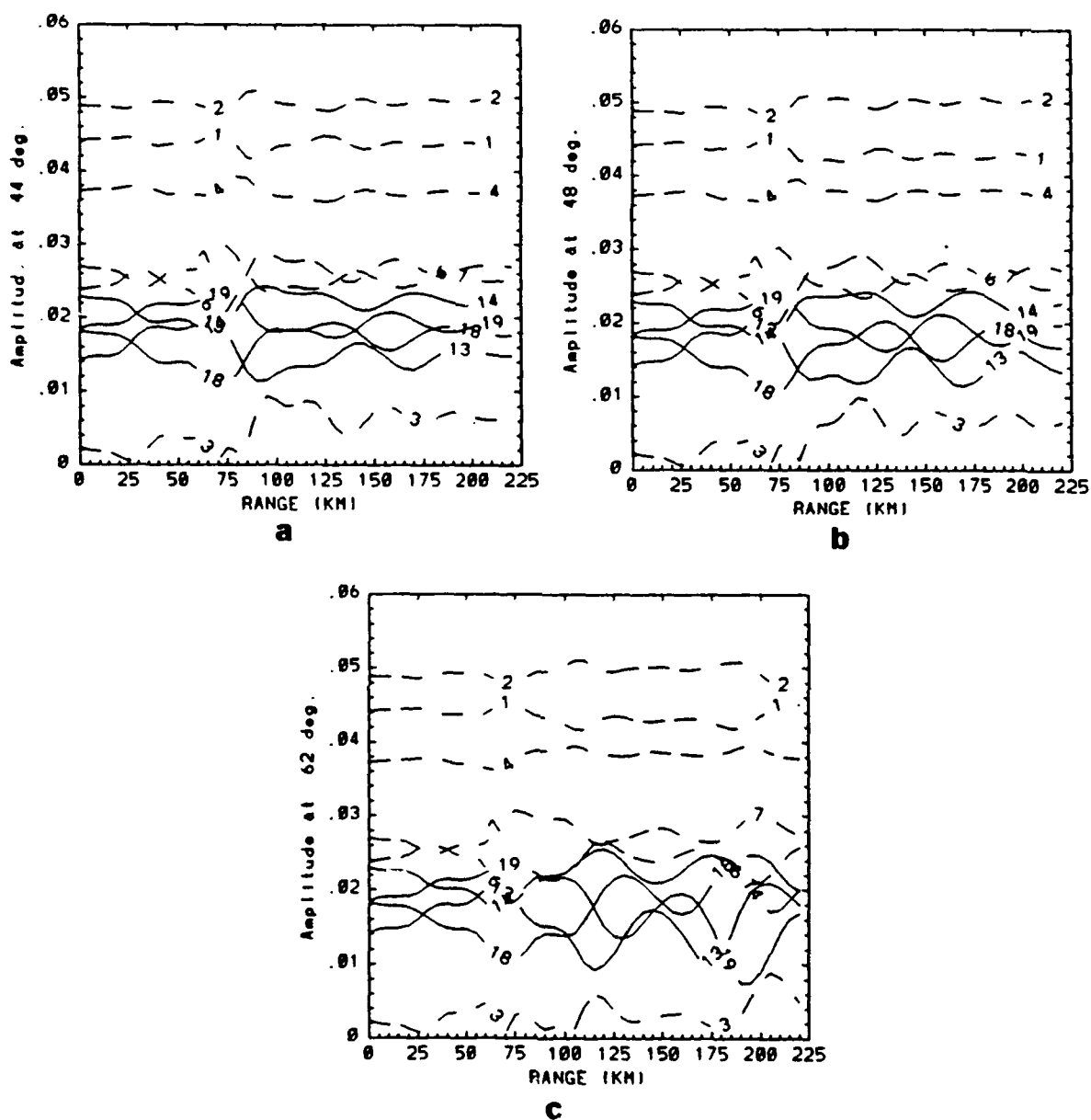


Figure 3.2: Envelope Amplitude of 10 Modes from the 3-D CM Solution Along the Paths $\theta = 4^\circ$ (Figure 3.2a), $\theta = 48^\circ$ (Figure 3.2b), and $\theta = 62^\circ$ (Figure 3.2c). (Source is placed outside a warm eddy at depth = 1360 m)

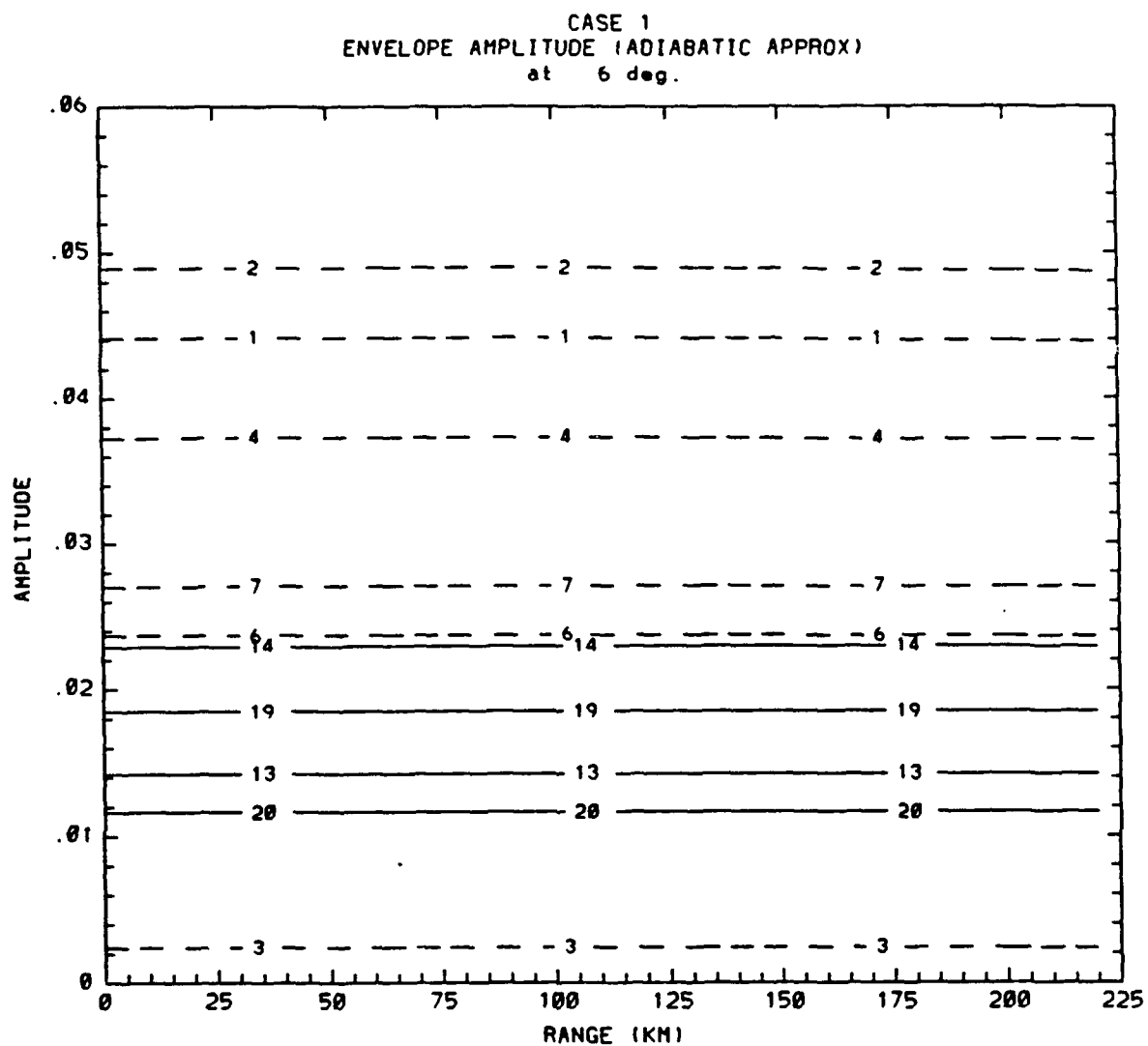


Figure 3.3: Envelope Amplitude of 10 modes for the 3-D Adiabatic Approximation Solution Along the Path $\theta = 6^\circ$. (Source is placed outside a warm eddy at depth = 1360 m)

PHASE DIFFERENCE (3D - AA)

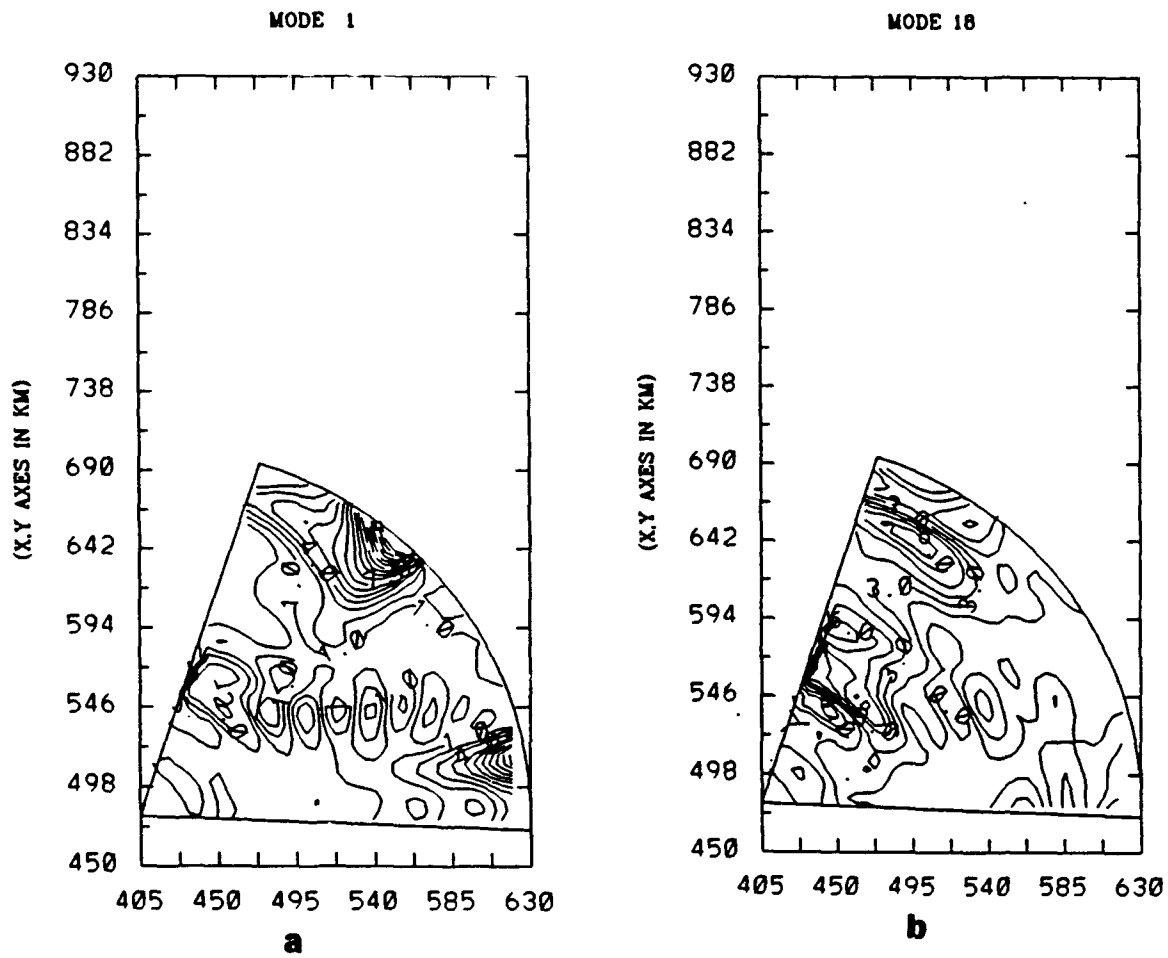


Figure 3.4: Differences Between the Phases of the 3-D CM and Adiabatic Solutions for Modes 1 (Figure 3.4a) and 18 (Figure 3.4b) at 1° Contour Interval. (Source is placed outside a warm eddy at depth = 1360 m)

CASE 1
ENVELOPE AMPLITUDE (3-D COUPLED MODE)

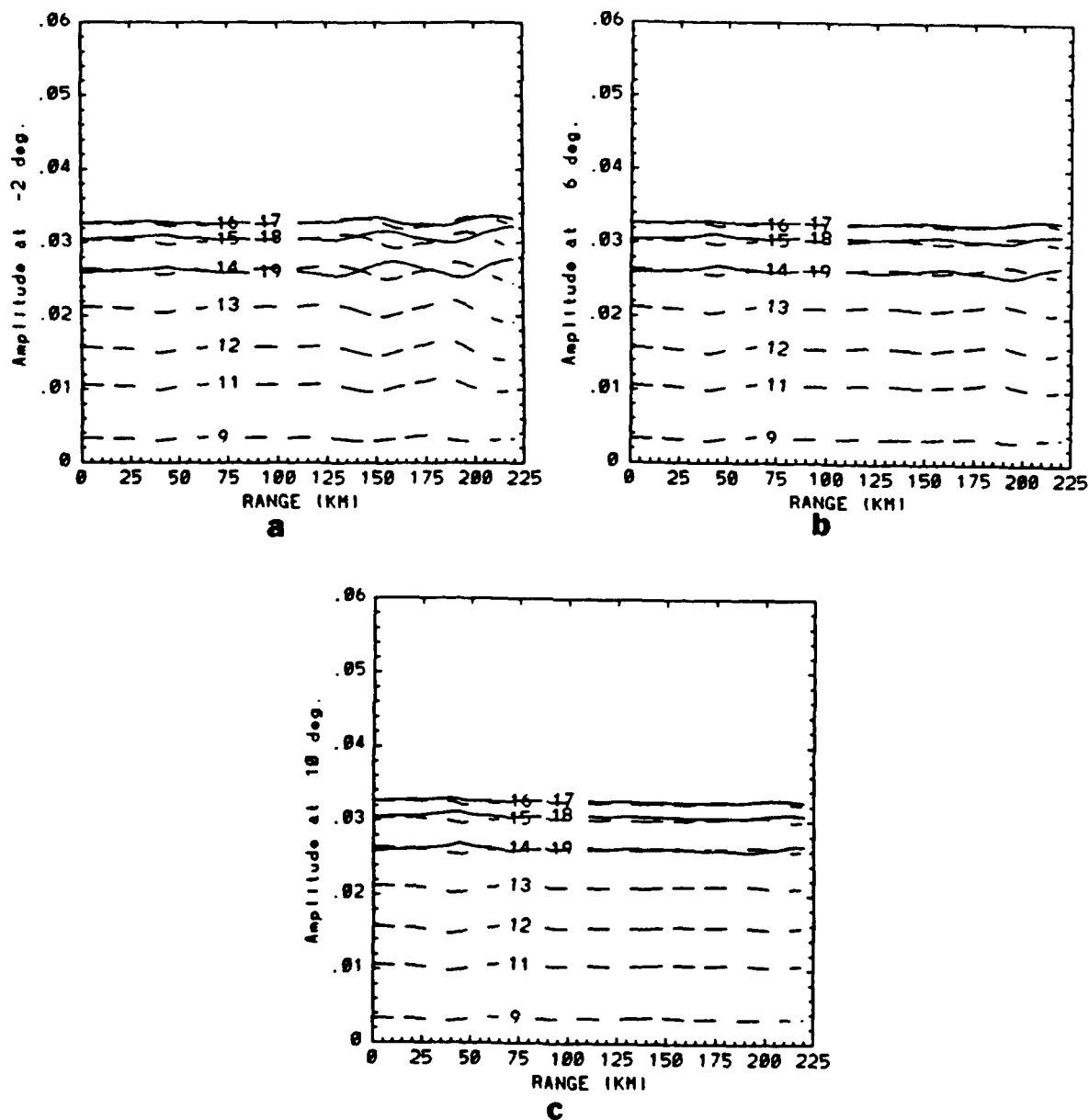


Figure 3.5: Envelope Amplitude of 20 Modes from the 3-D CM Solution Along the Paths $\theta = -2^\circ$ (Figure 3.5a), $\theta = 6^\circ$ (Figure 3.5b), and $\theta = 10^\circ$ (Figure 3.5c). (Source is placed outside a warm eddy at depth = 300 m)

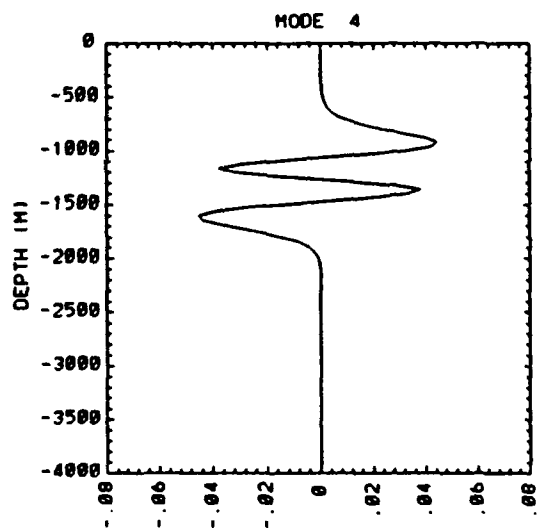
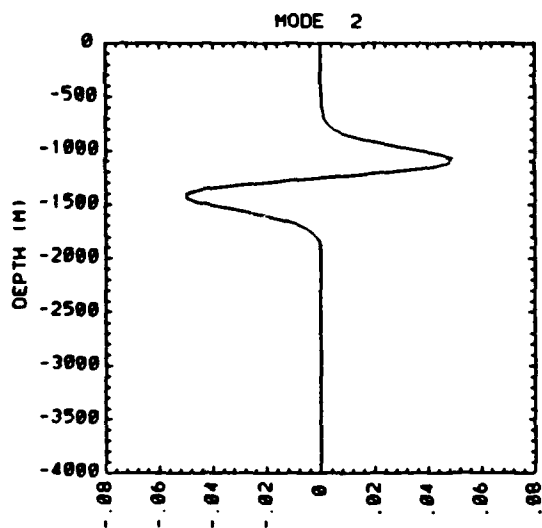
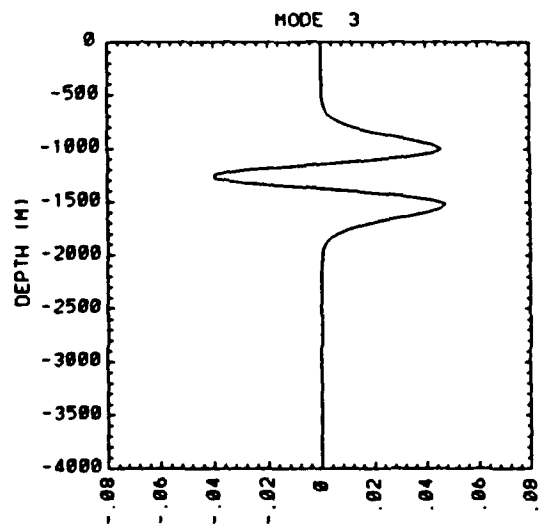
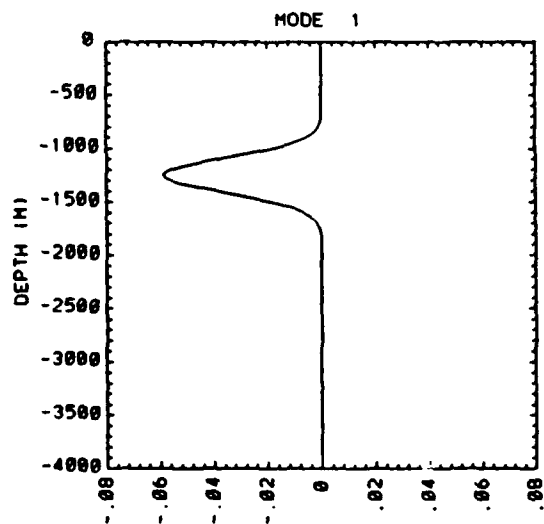


Figure 3.6: Eigenfunctions Calculated for Modes 1 to 4 at a Horizontal Location

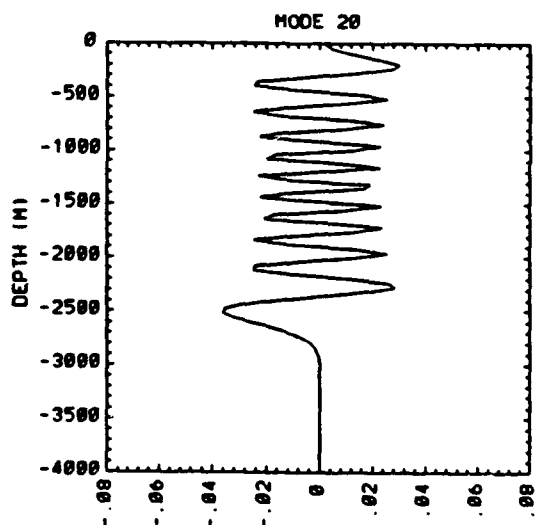
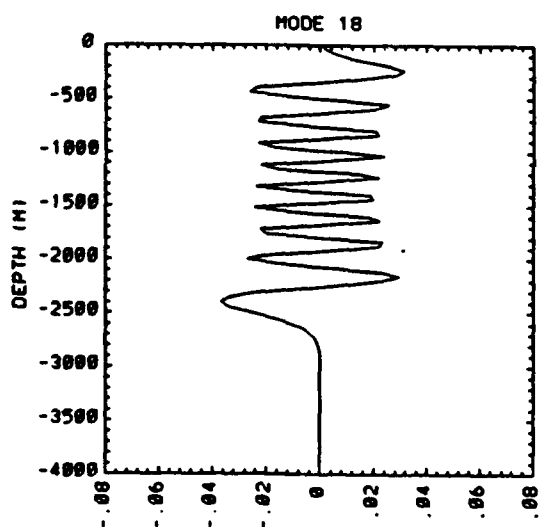
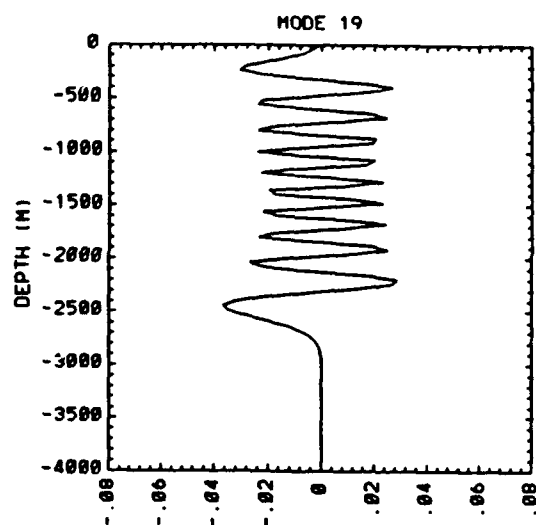
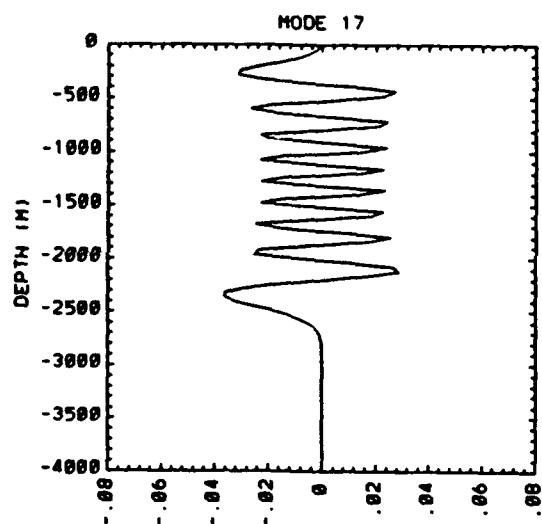


Figure 3.7: Eigenfunctions Calculated for Modes 17 to 20 at a Horizontal Location

CASE 1
ENVELOPE AMPLITUDE (3-D COUPLED MODE)

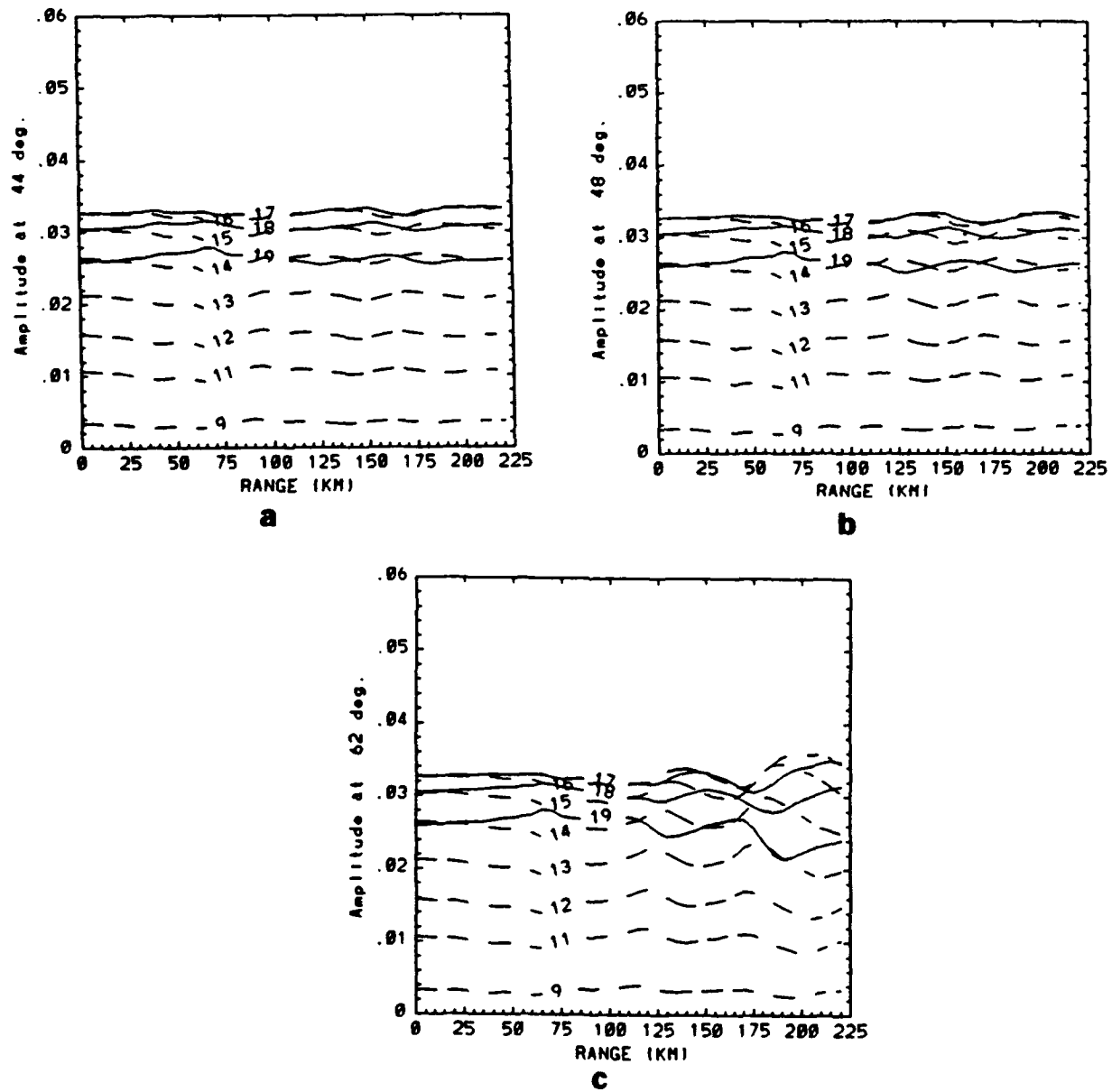


Figure 3.8: Envelope Amplitude of 20 Modes in the 3-D CM Solution Along the Paths $\theta = 44^\circ$ (Figure 3.8a), $\theta = 48^\circ$ (Figure 3.8b), and $\theta = 62^\circ$ (Figure 3.8c). (Source is placed outside warm eddy at depth = 300 m)

PHASE DIFFERENCE (3D - AA)

MODE 17

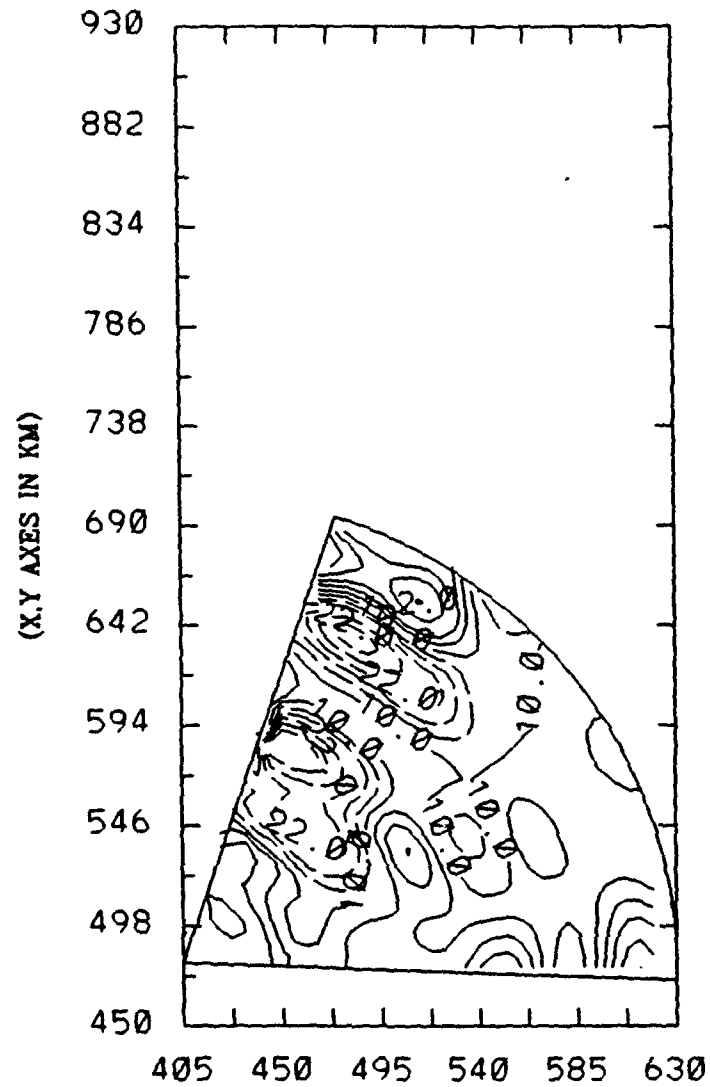


Figure 3.9: Differences Between the Phases of Mode 17 in the 3-D CM and Adiabatic Approximation Results Over the Entire Solution Domain at Contour Interval $\approx 4^\circ$. (Source is placed outside warm eddy at depth = 300 m)

TRANSMISSION LOSS (3D - AA) AT 6 DEG.

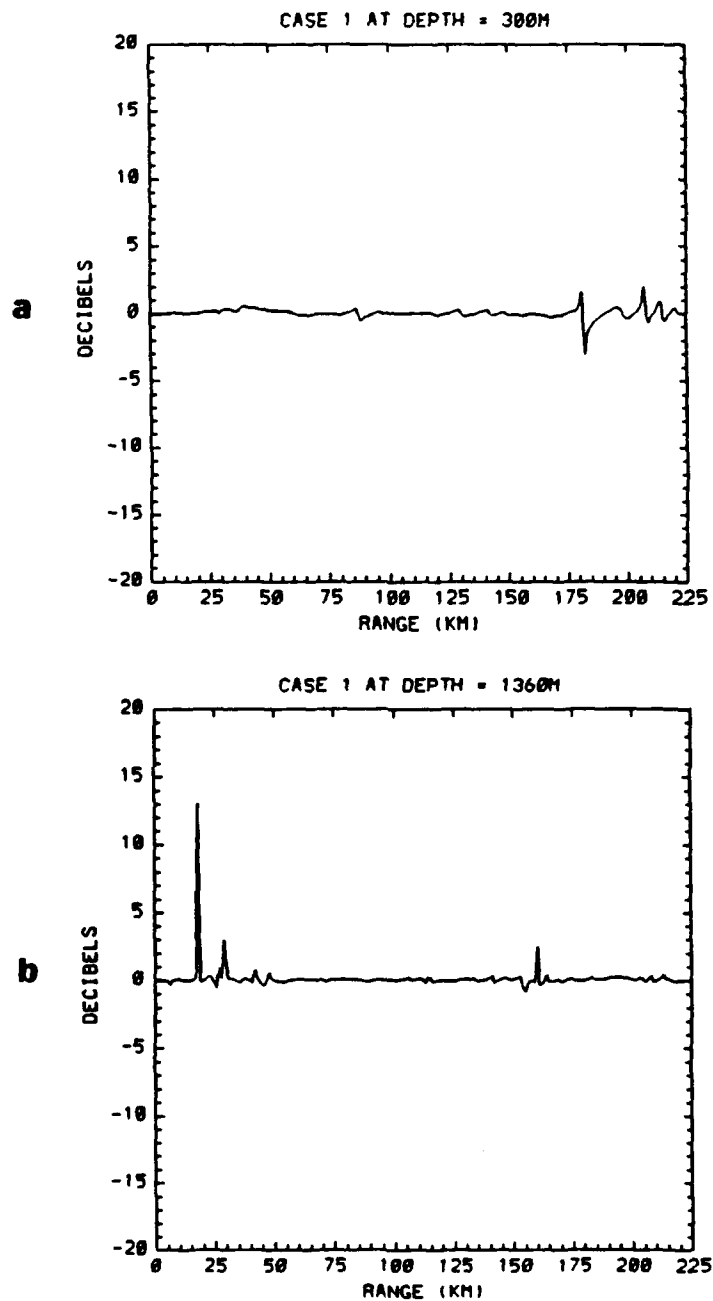


Figure 3.10: Differences in Transmission Loss Between the 3-D CM and Adiabatic Results at 300 m depth (Figure 3.10a) and 1360 m depth (Figure 3.10b) along the Path $\theta = 6^\circ$. (Source is placed outside warm eddy for depths of 300 m (Figure 3.6a) and 1360 m (Figure 3.6b))

TRANSMISSION LOSS (3D - AA) AT 48 DEG.

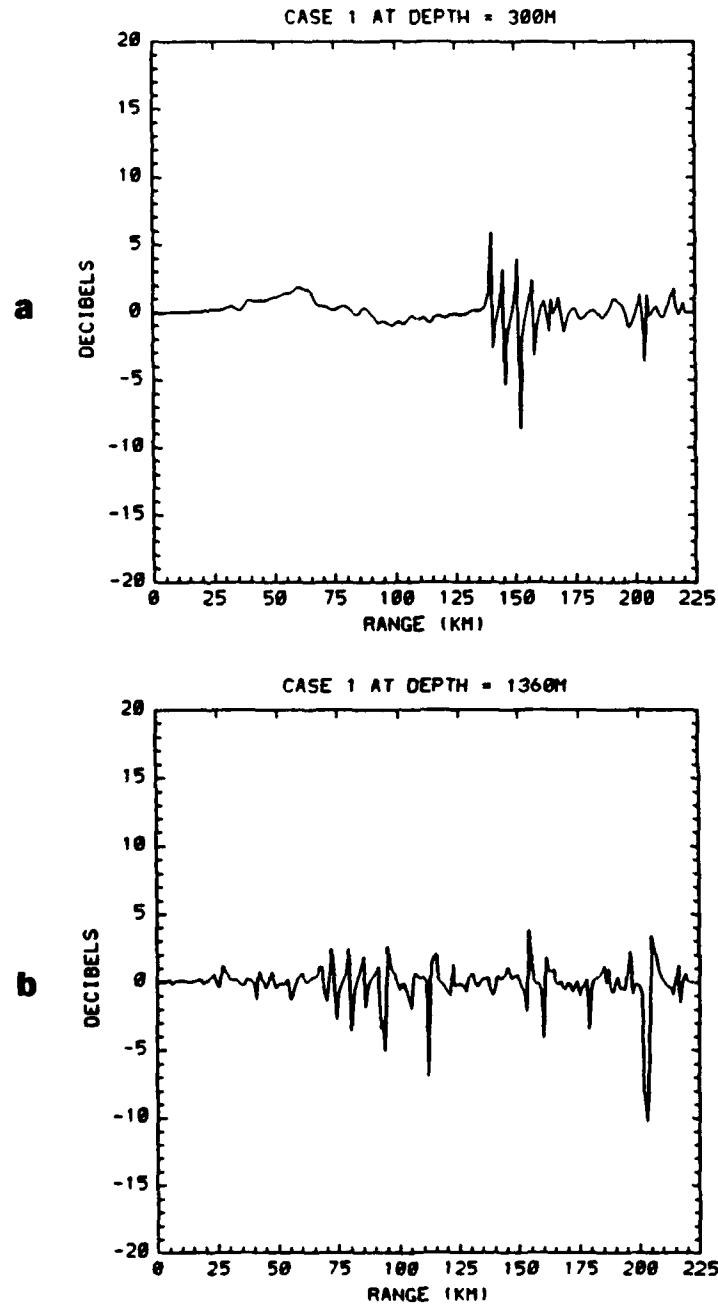


Figure 3.11: Differences in Transmission Loss Between the 3-D CM and Adiabatic Results at 300 m depth (Figure 3.11a) and 1360 m depth (Figure 3.11b) along the Path $\theta = 48^\circ$. (Source is placed outside of warm eddy for depths of 300 m (Figure 3.11a) and 1360 m (Figure 3.11b))

TRANSMISSION LOSS (3D - AA) AT 62 DEG.

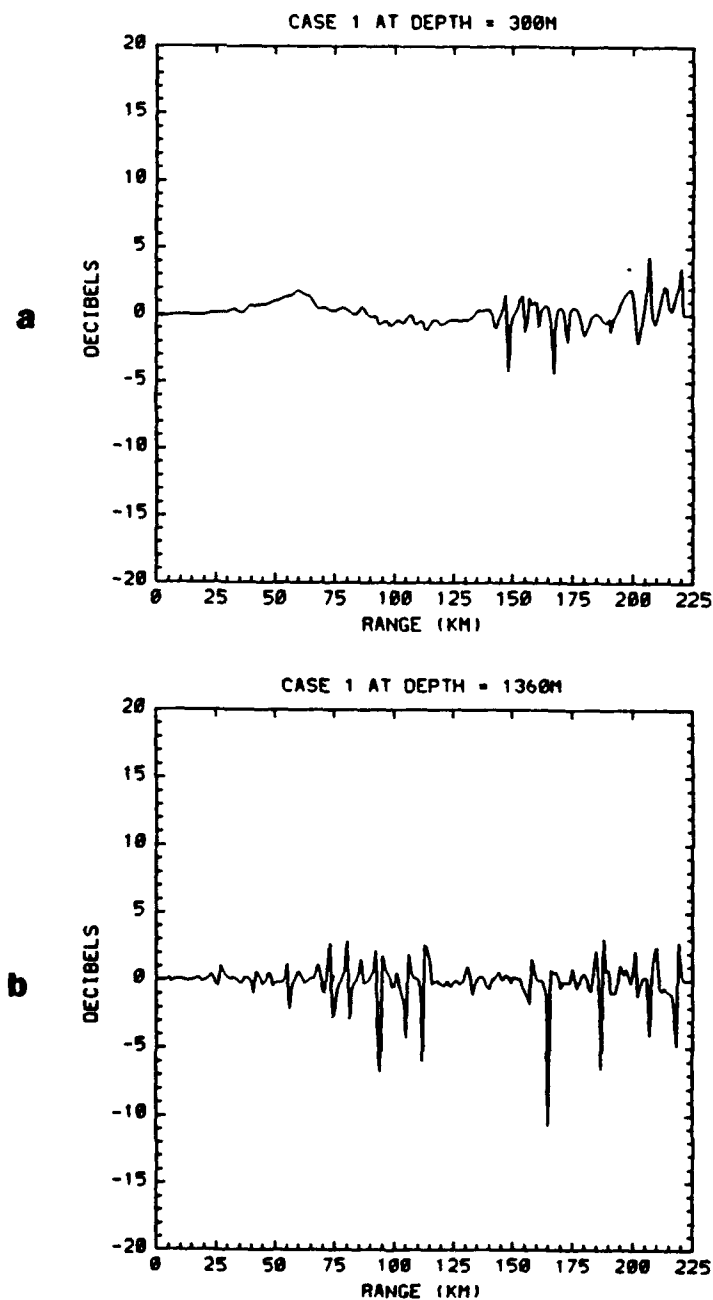


Figure 3.12: Differences in Transmission Loss Between the 3-D CM and Adiabatic Results at 300 m depth (Figure 3.12a) and 1360 m depth (Figure 3.12b) along the Path $\theta = 62^\circ$. (Source is placed outside of warm eddy for depths of 300 m (Figure 3.12a) and 1360 m (Figure 3.12b))

AMPLITUDE DIFFERENCE

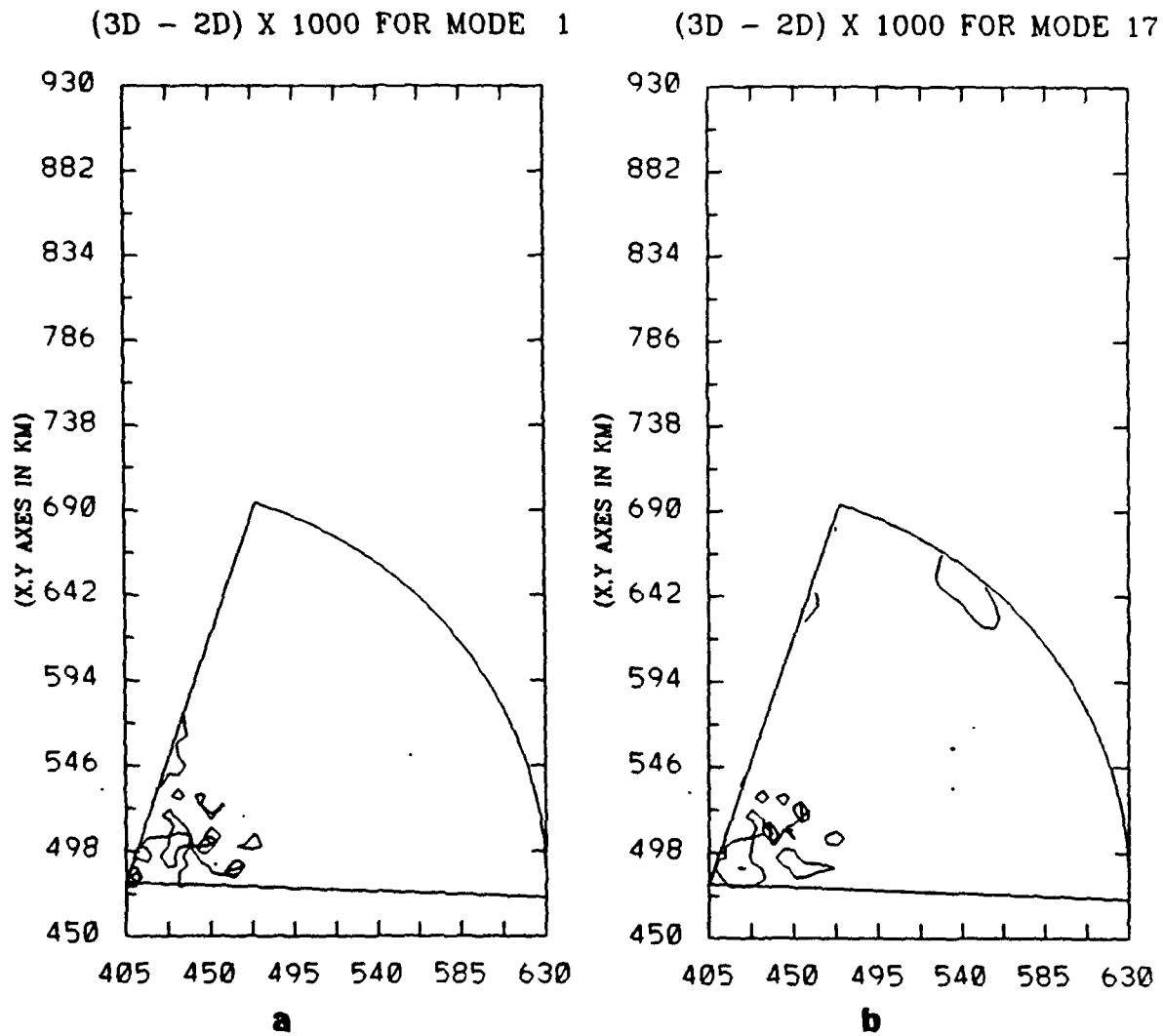


Figure 3.13: Differences Between the Amplitudes of the 3-D CM and Nx2-D Solutions for Modes 1 (Figure 3.13a) and Mode 17 (Figure 3.13b) at Contour Interval = 1 x 1000. (Source is placed outside warm eddy at depth = 1360 m)

PHASE DIFFERENCE (3D - 2D)

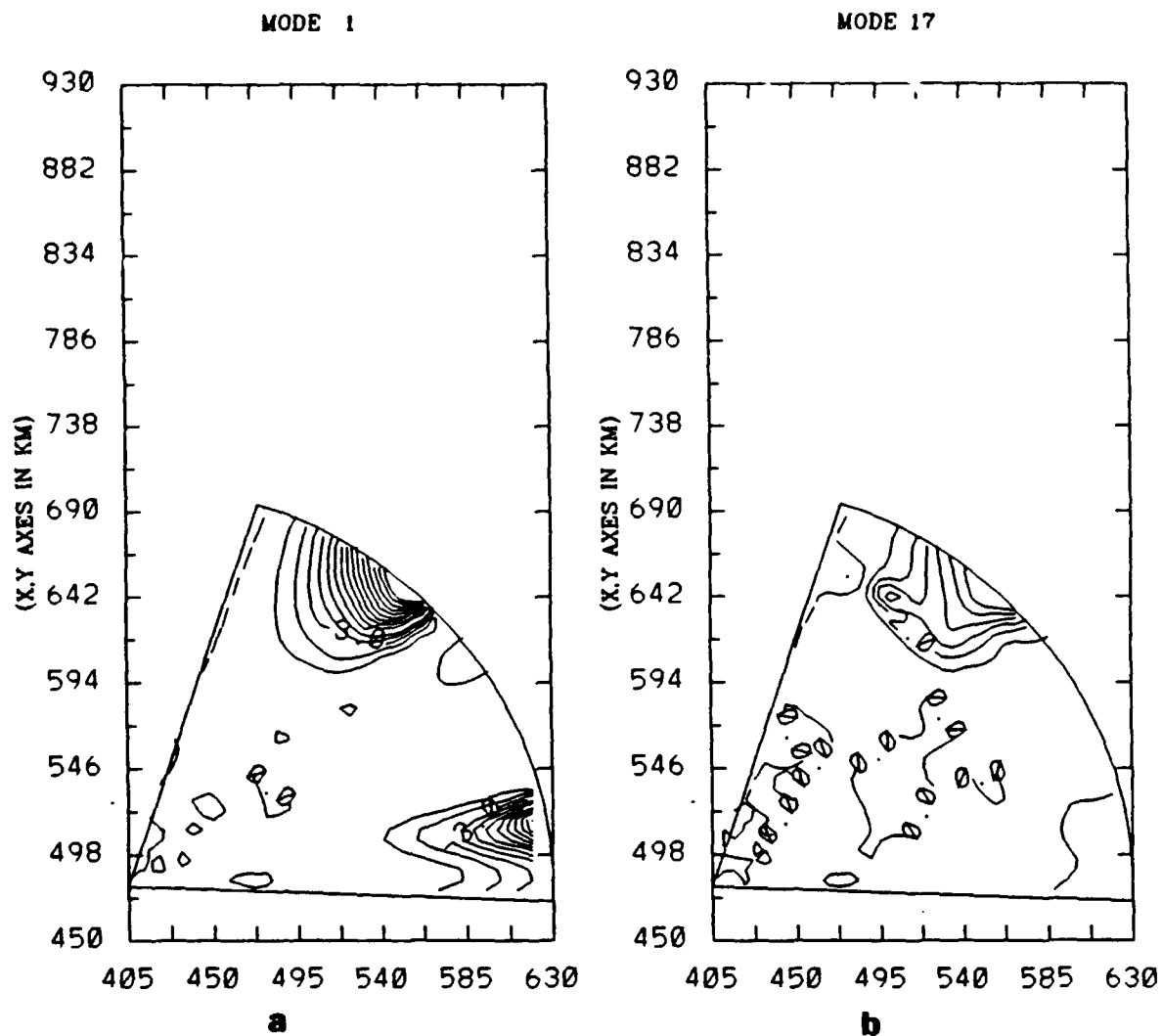


Figure 3.14: Differences Between the Phases of the 3-D CM and Nx2-D Solutions for Modes 1 (Figure 3.14a) and 17 (Figure 3.14b) at Contour Interval = 1° . (Source is placed outside warm eddy at depth = 1360 m)

AMPLITUDE DIFFERENCE

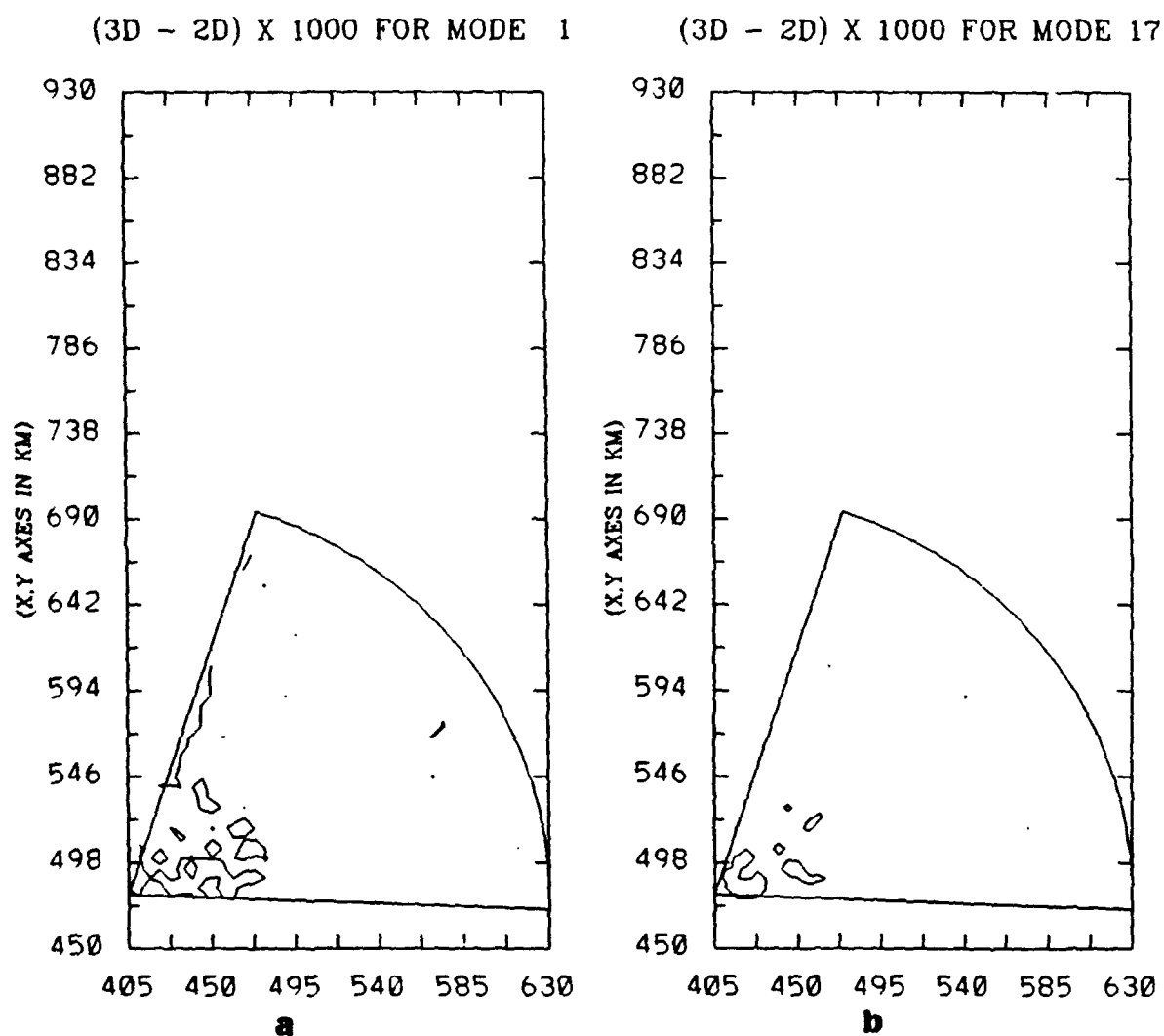


Figure 3.15: Difference Between the Amplitudes of the 3-D and Nx2-D Solutions for Modes 1 (Figure 3.15a) and 17 (Figure 3.15b). (Source is placed outside a warm eddy at depth = 300 m)

PHASE DIFFERENCE (3D - 2D)

MODE 17

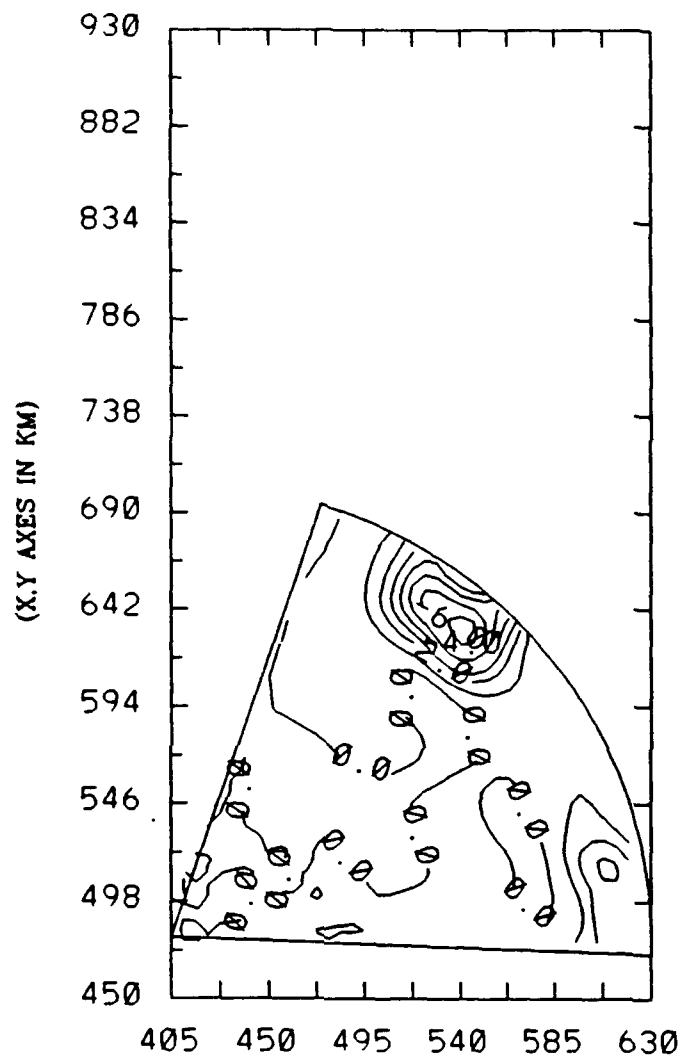


Figure 3.16: Differences Between the Phases of Mode 17 in the 3-D CM and Nx2-D Solutions Over the Entire Solution Domain at Contour Interval = 1°. (Source is placed outside warm eddy at depth = 300 m)

TRANSMISSION LOSS (3D - 2D) AT 6 DEG.

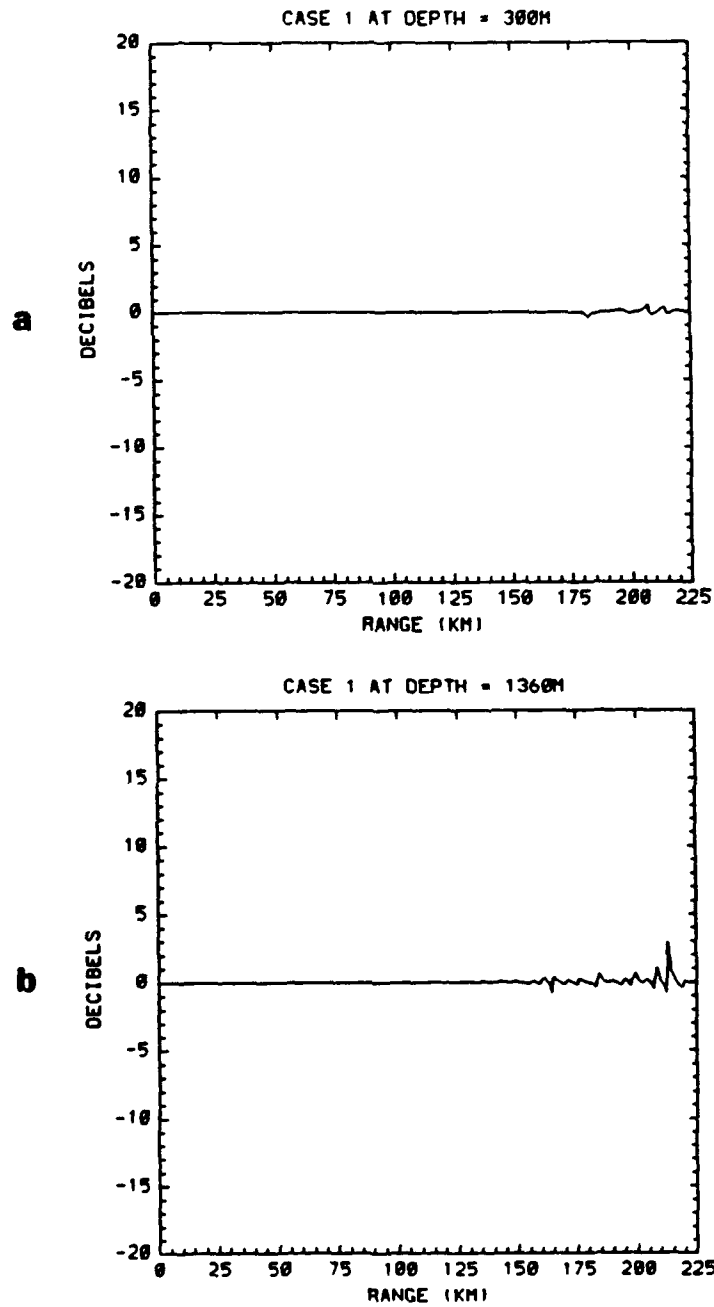


Figure 3.17: Differences in Transmission Loss Between the 3-D CM and Nx2-D Results at 300 m Depth (Figure 3.17a) and 1360 m depth (Figure 3.17b) along the Path $\theta = 6^\circ$. (Source is placed inside warm eddy for depths of 300 m (Figure 3.17a) and 1360 m (Figure 3.17b))

TRANSMISSION LOSS (3D - 2D) AT 48 DEG.

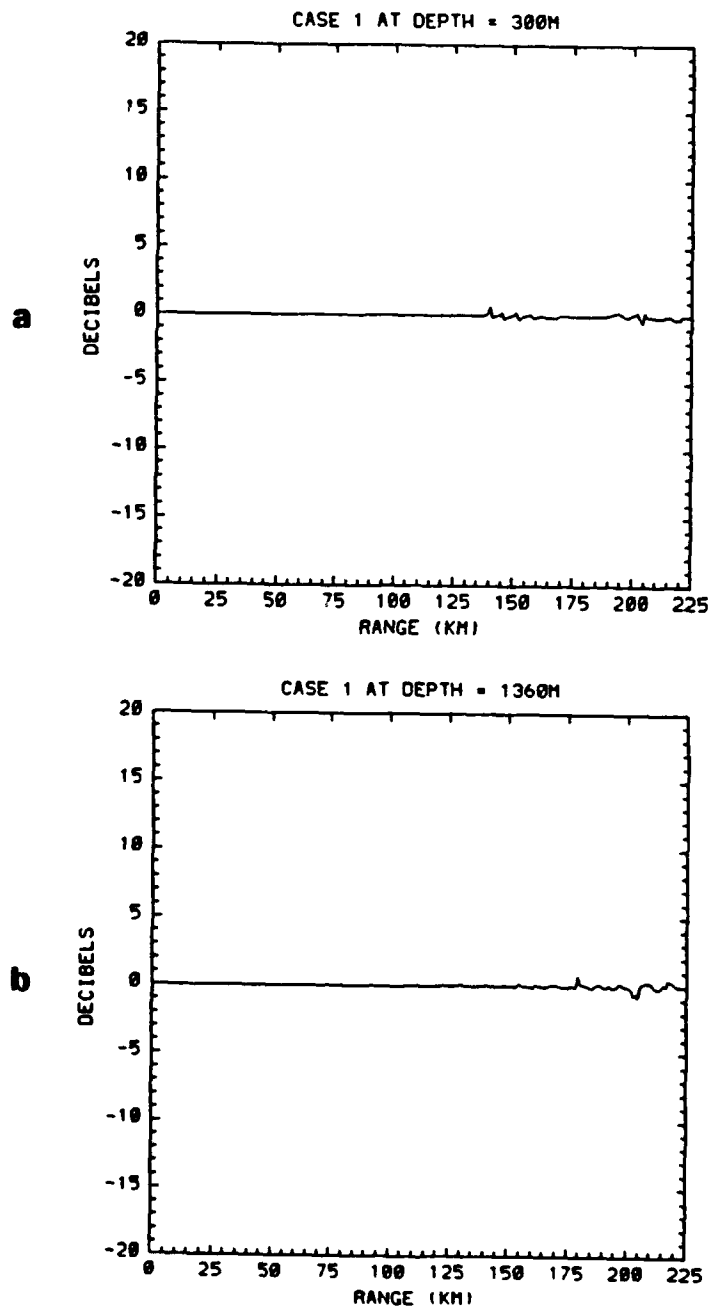


Figure 3.18: Differences in Transmission Loss Between the 3-D CM and Nx2-D Results at 300 m Depth (Figure 3.18a) and 1360 m depth (Figure 3.18b) along the Path $\theta = 48^\circ$. (Source is placed inside warm eddy for depths of 300 m (Figure 3.18a) and 1360 m (Figure 3.18b))

TRANSMISSION LOSS (3D - 2D) AT 62 DEG.

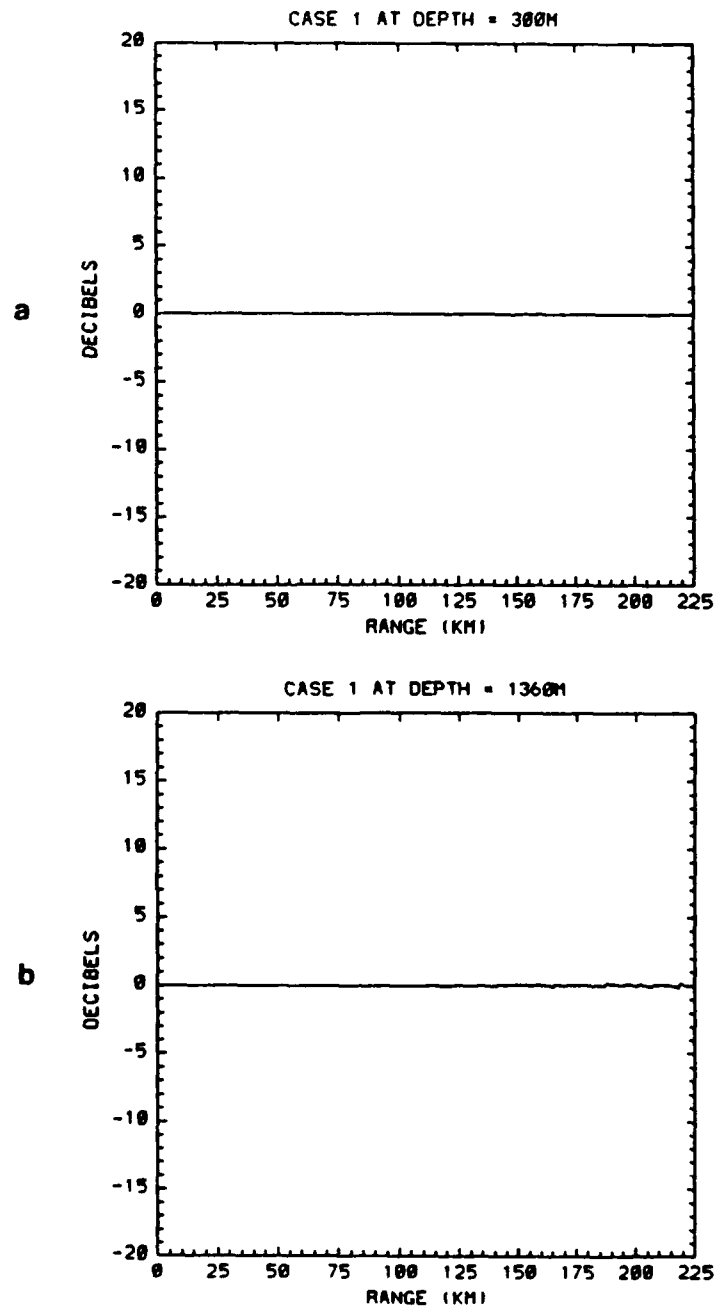


Figure 3.19: Differences in Transmission Loss Between the 3-D CM and Nx2-D Results at 300 m Depth (Figure 3.19a) and 1360 m depth (Figure 3.19b) along the Path $\theta = 62^\circ$. (Source is placed inside warm eddy for depths of 300 m (Figure 3.19a) and 1360 m (Figure 3.19b))

CASE 2
ENVELOPE AMPLITUDE (3-D COUPLED MODE)

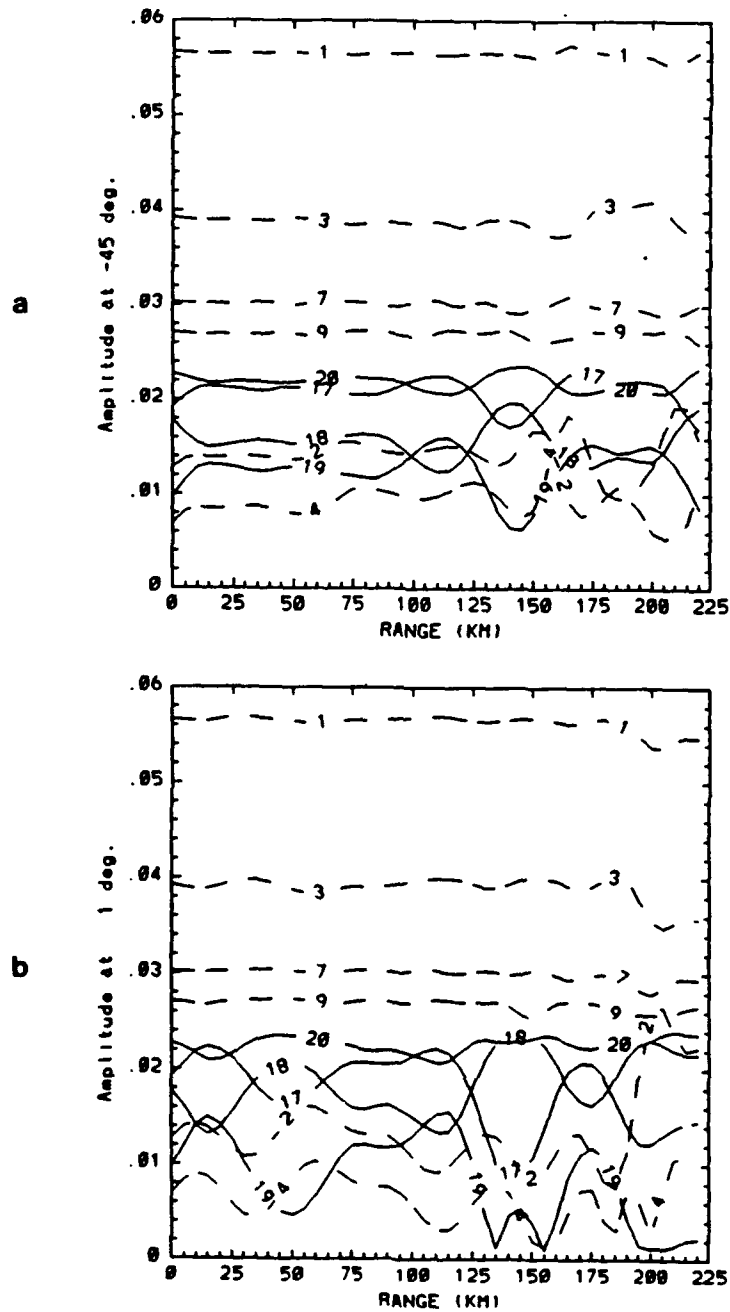


Figure 3.20: Envelope Amplitudes of 10 of the Modes in the 3-D CM Solution Along the Paths $\theta = -45^\circ$ (Figure 3.20a) and $\theta = 1^\circ$ (Figure 3.20b). (Source is placed inside warm eddy at depth = 1360 m)

AMPLITUDE DIFFERENCE

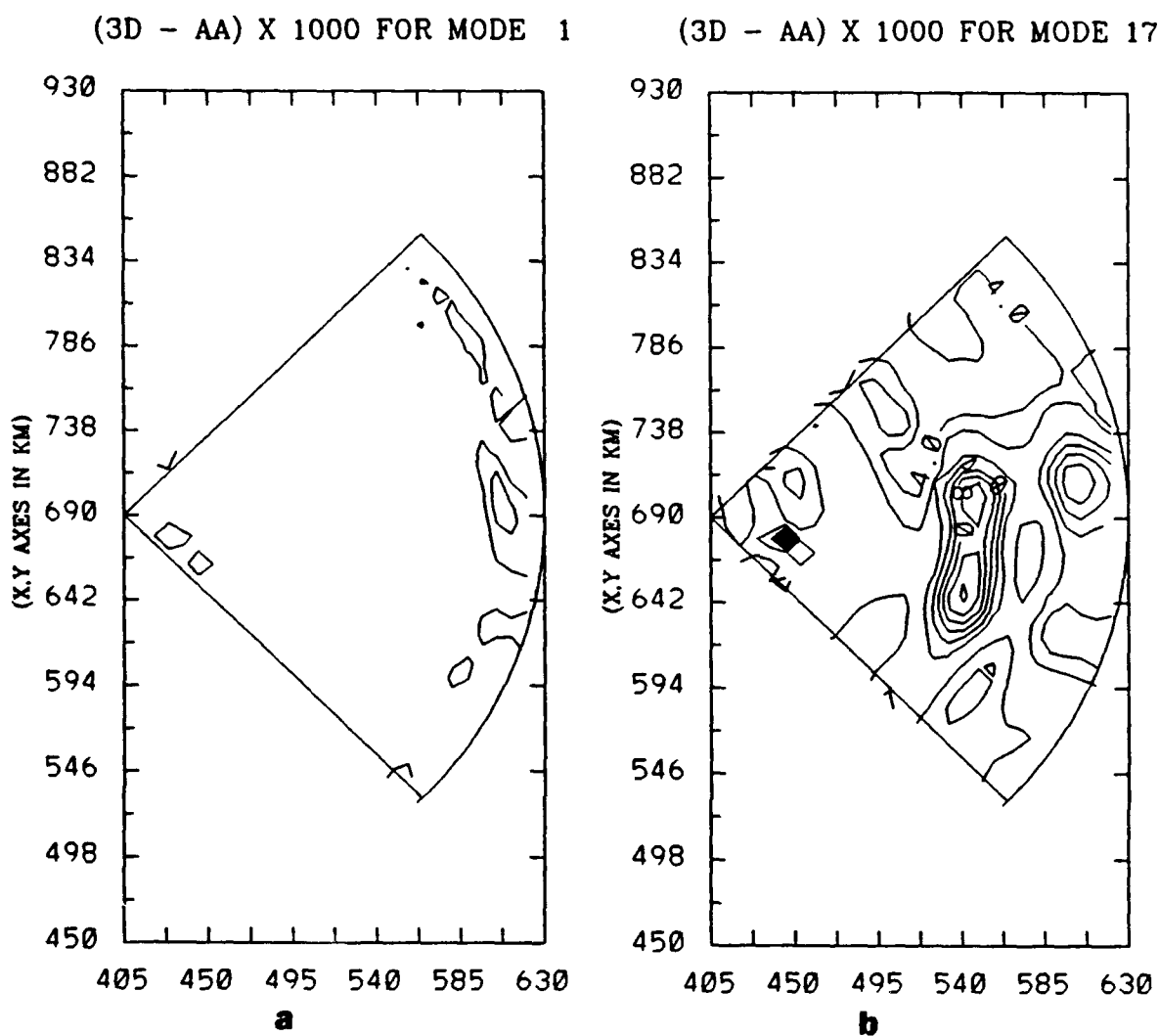


Figure 3.21: Differences Between the Envelope Amplitudes of the 3-D CM and Adiabatic Solutions for Mode 1 at Contour Interval = 1 (Figure 3.21a) and Mode 17 at Contour Interval = 2 (Figure 3.21b). (Source is placed inside warm eddy at depth = 1360 m)

PHASE DIFFERENCE (3D - AA)

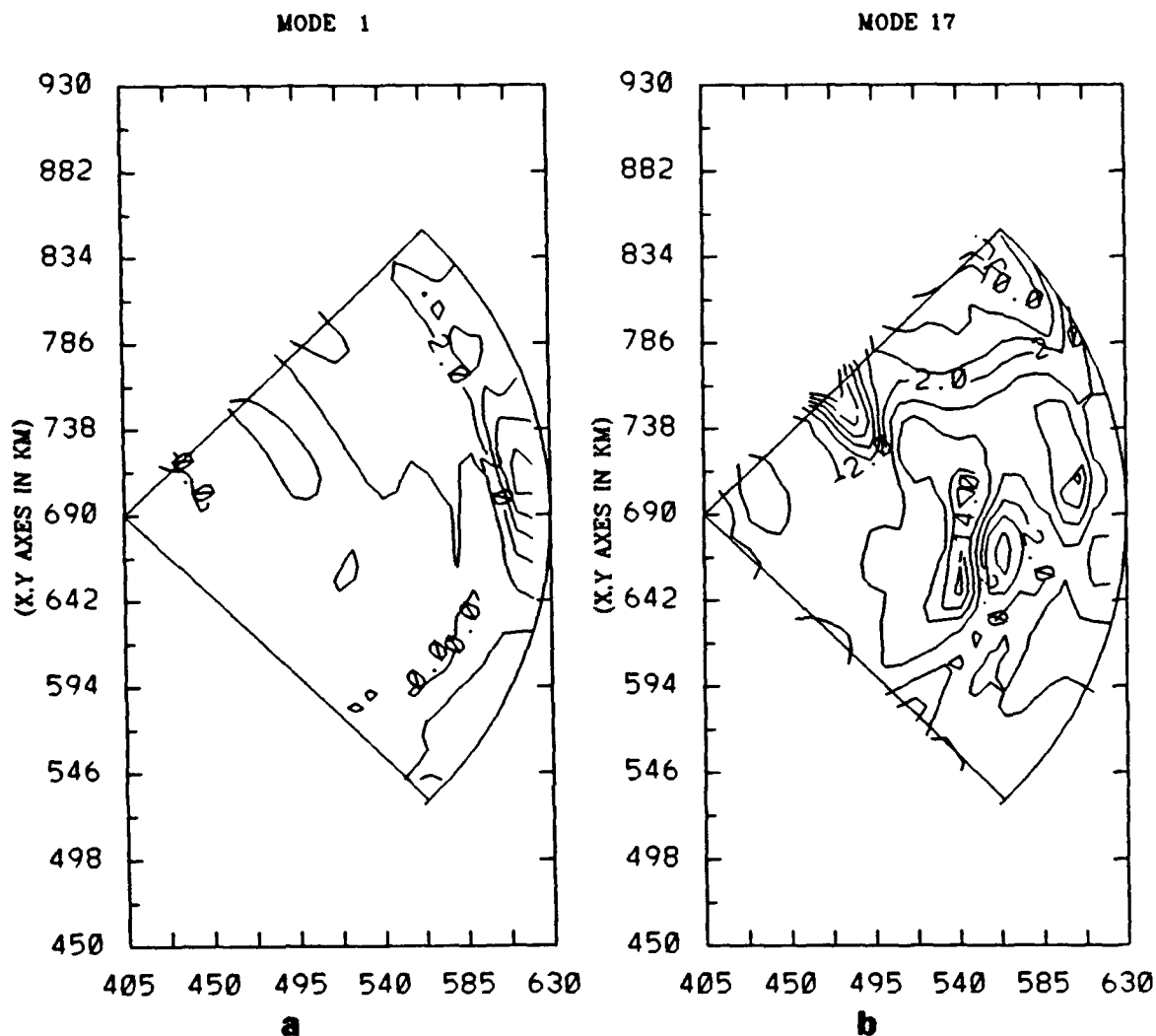


Figure 3.22: Differences Between the Phases of the 3-D CM and Adiabatic Approximation for Mode 1 at Contour Interval = 1° (Figure 3.22a) and Mode 17 at Contour Interval = 4° (Figure 3.22b). (Source is placed inside warm eddy at depth = 1360 m)

CASE 2
ENVELOPE AMPLITUDE (3-D COUPLED MODE)

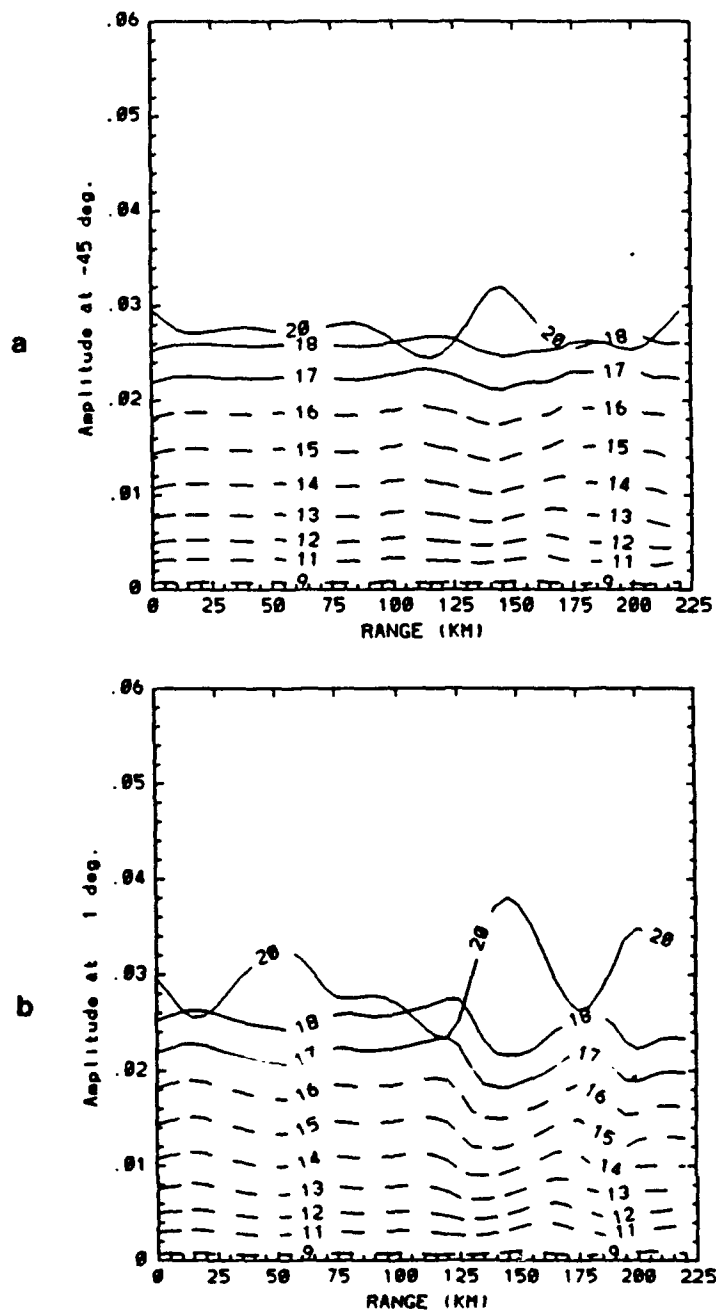


Figure 3.23: Envelopes Amplitudes of 10 of the Modes in the 3-D CM Solution Along the Paths $\theta = -45^\circ$ (Figure 3.23a) and $\theta = 1^\circ$ (Figure 3.23b). (source is placed inside warm eddy at depth = 300 m)

AMPLITUDE DIFFERENCE

(3D - AA) X 1000 FOR MODE 17

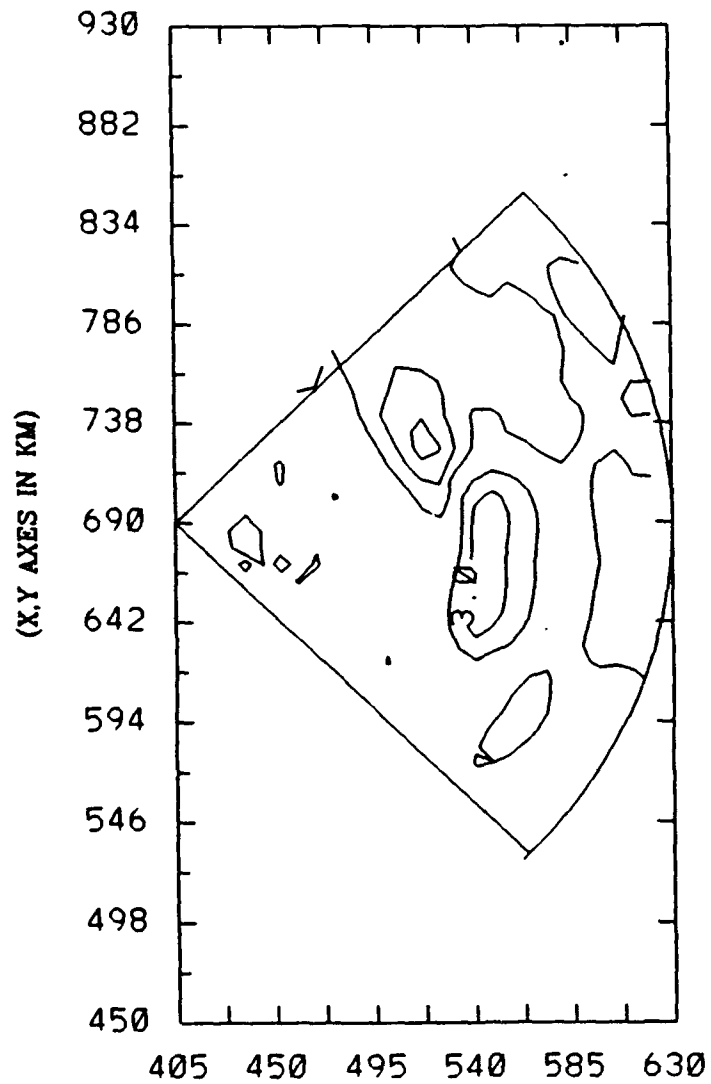


Figure 3.24: Differences Between the Envelope Amplitudes of Modes 17 in the 3-D CM and Adiabatic Approximation over the Entire Solution Domain at Contour Interval = 4. (Source is placed inside warm eddy at depth = 300 m)

PHASE DIFFERENCE (3D - AA)

MODE 17

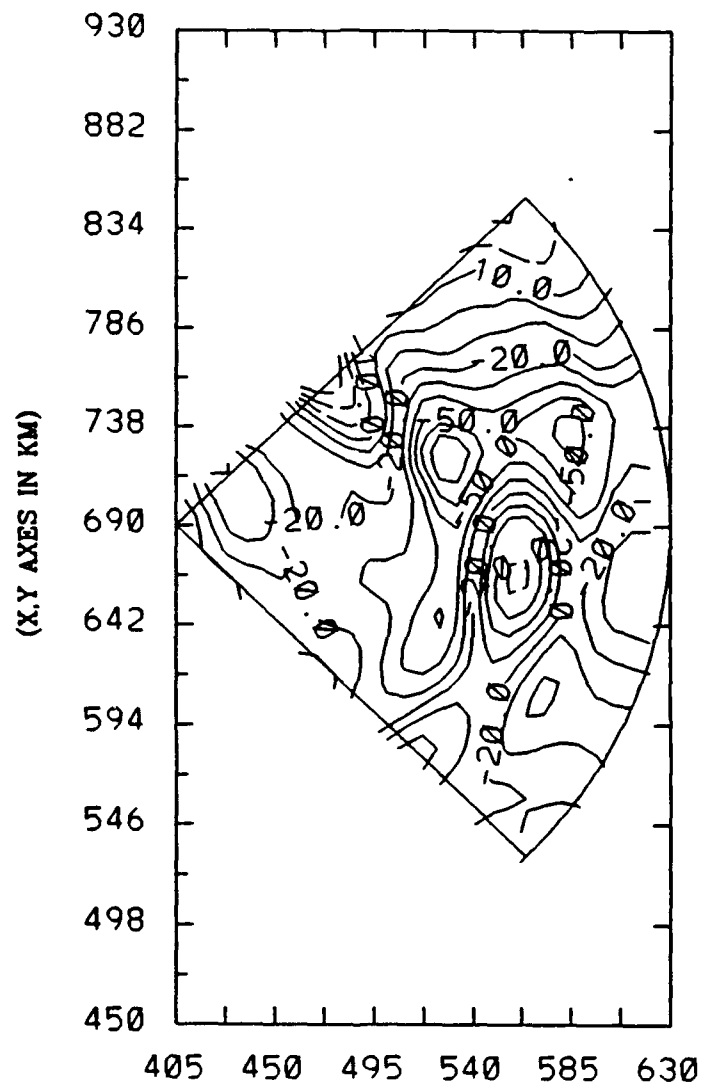


Figure 3.25: Differences Between the Phases of Mode 17 in the 3-D CM and Adiabatic Results over the Entire Solution Domain at Contour Interval = 10°. (Source is placed inside the warm eddy at depth = 300 m)

TRANSMISSION LOSS (3D - AA) AT -45 DEG.

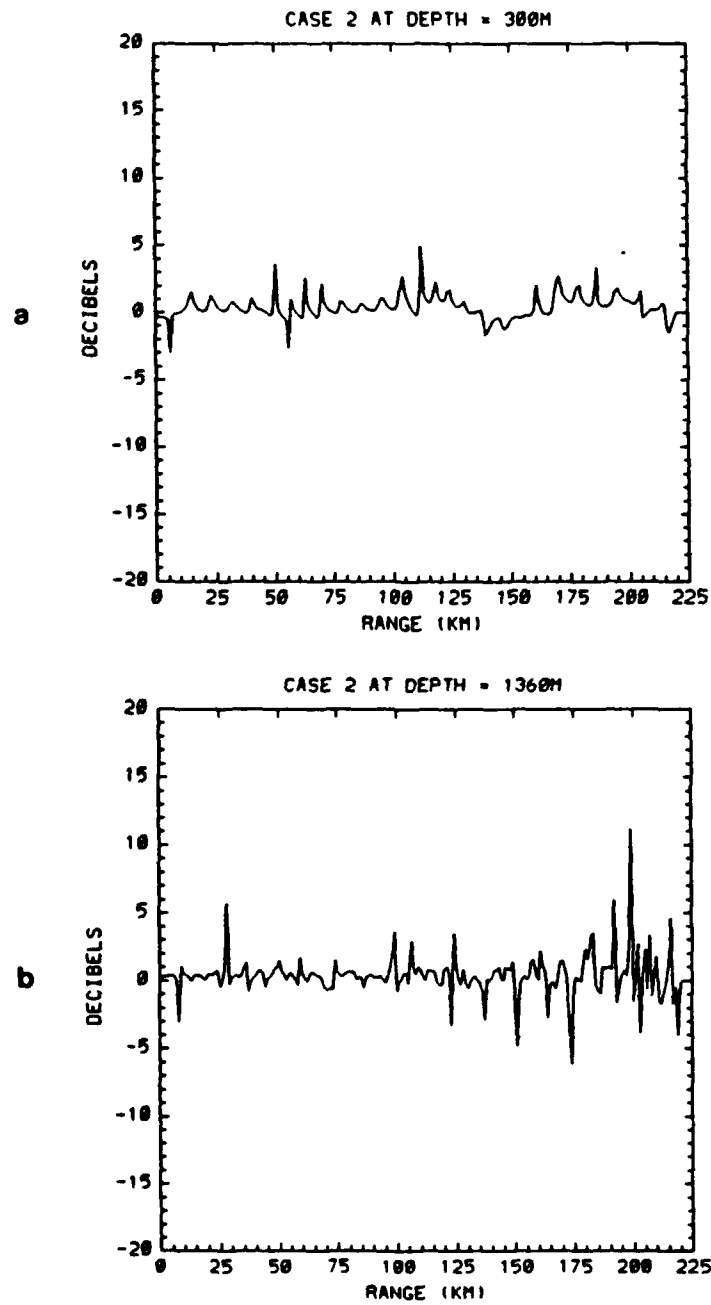


Figure 3.26: Differences in Transmission Loss Between the 3-D CM and Adiabatic Approximation Results at 300 m depth (Figure 3.26a) and 1360 m depth (Figure 3.26b) along the Path $\theta = -45^\circ$. (Source is placed inside warm eddy for depths of 300 m (Figure 3.26a) and 1360 m (Figure 3.26b))

TRANSMISSION LOSS (3D - AA) AT 1 DEG.

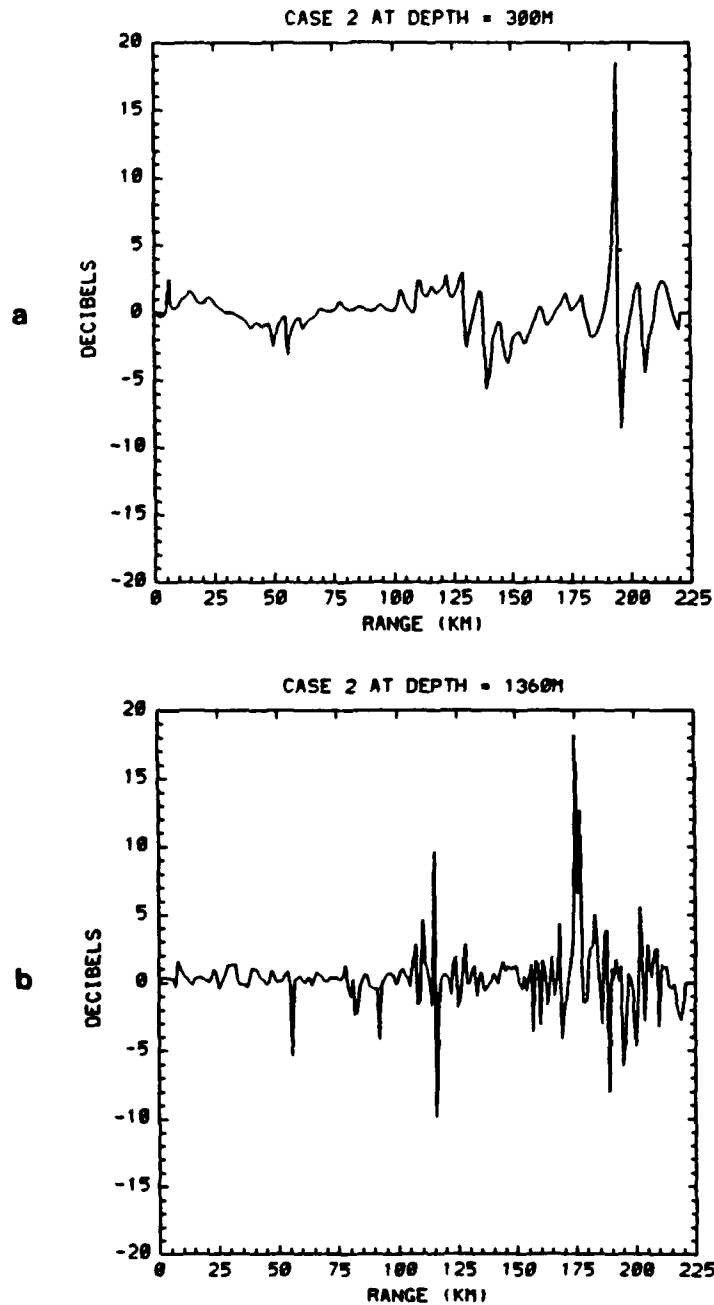


Figure 3.27: Differences in Transmission Loss Between the 3-D CM and Adiabatic Approximation Results at 300 m depth (Figure 3.27a) and 1360 m depth (Figure 3.27b) along the Path $\theta = 1^\circ$. (Source is placed inside warm eddy for depths of 300 m (Figure 3.27a) and 1360 m (Figure 3.27b))

PHASE DIFFERENCE (3D - 2D)

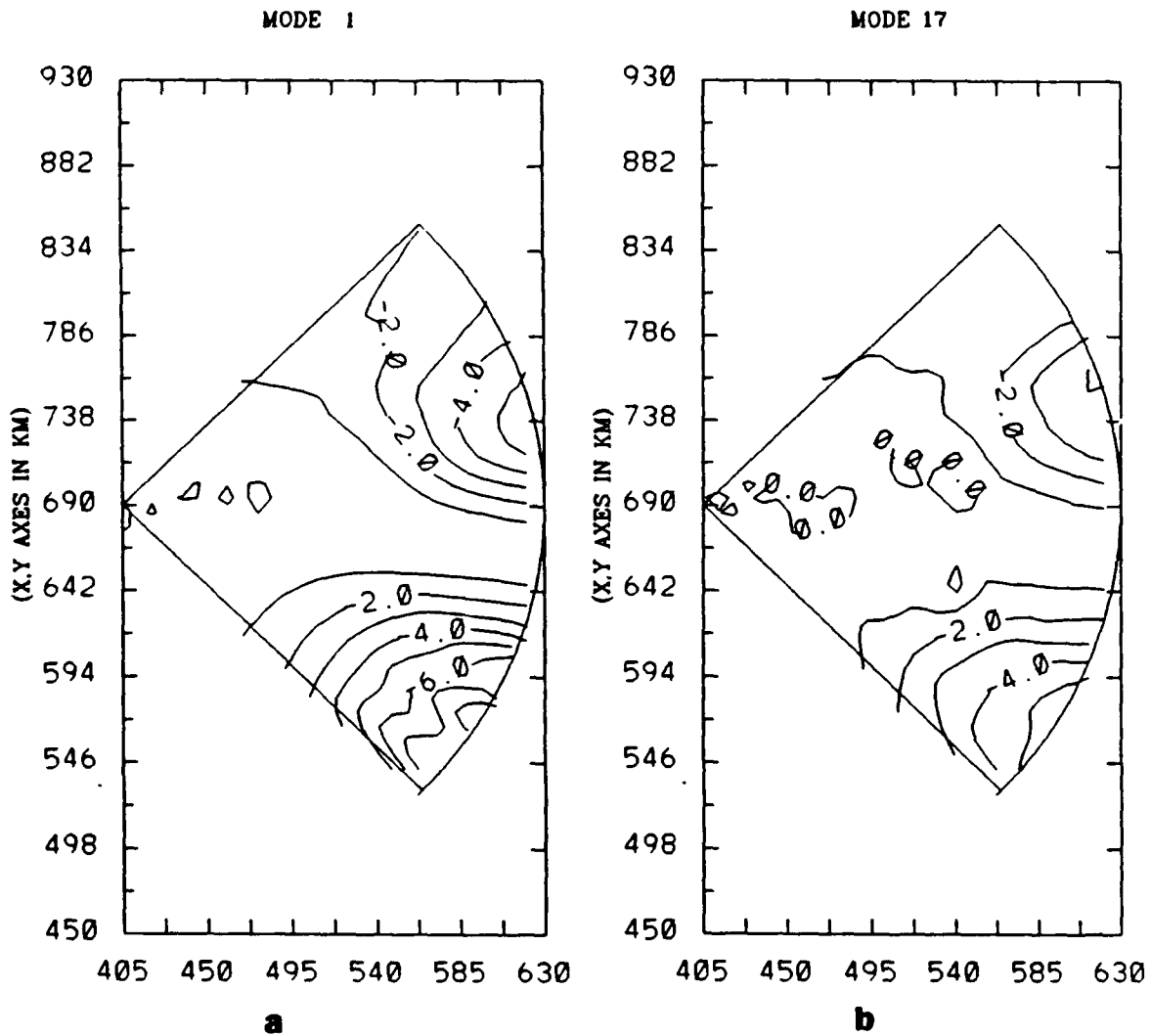


Figure 3.28: Differences Between the Phases of the 3-D CM and Nx2-D Solutions for Mode 1 (Figure 3.28a) and Mode 17 (Figure 3.28b). Contour Interval for both Graphs = 1°. (Source is inside warm eddy at depth = 1360 m)

PHASE DIFFERENCE (3D - 2D)

MODE 17

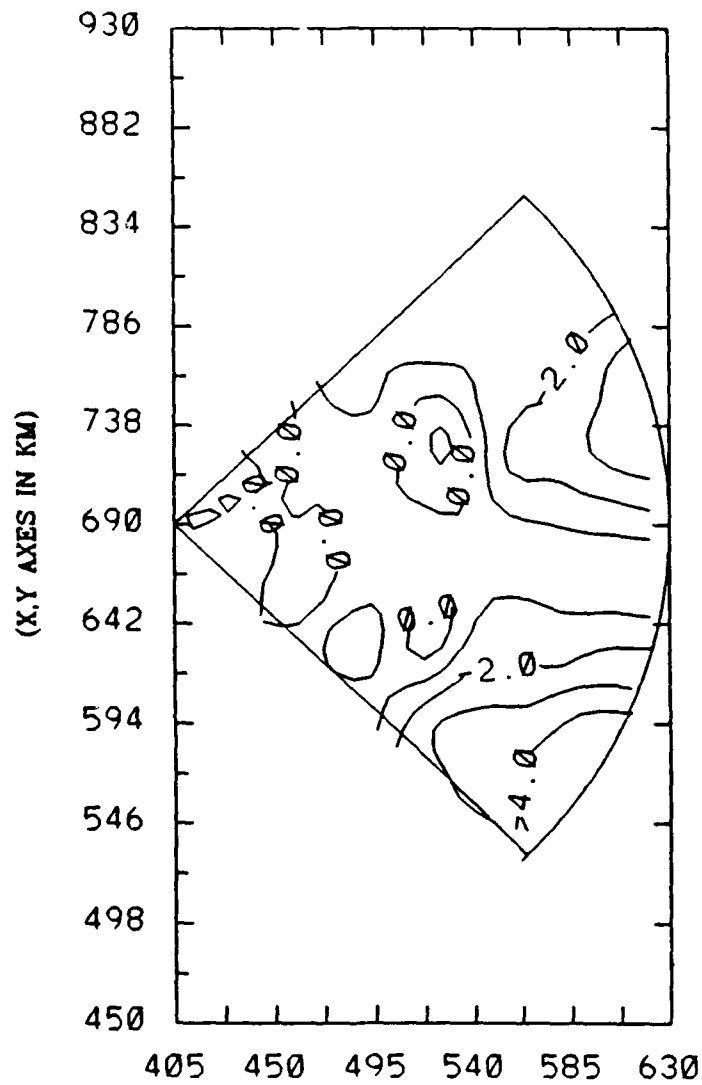


Figure 3.29: Differences Between the Phases of Mode 17 in the 3-D CM and Nx2-D Solutions at Contour Interval = 1°. (Source is placed inside warm eddy at depth = 300 m)

TRANSMISSION LOSS (3D - 2D) AT -45 DEG.

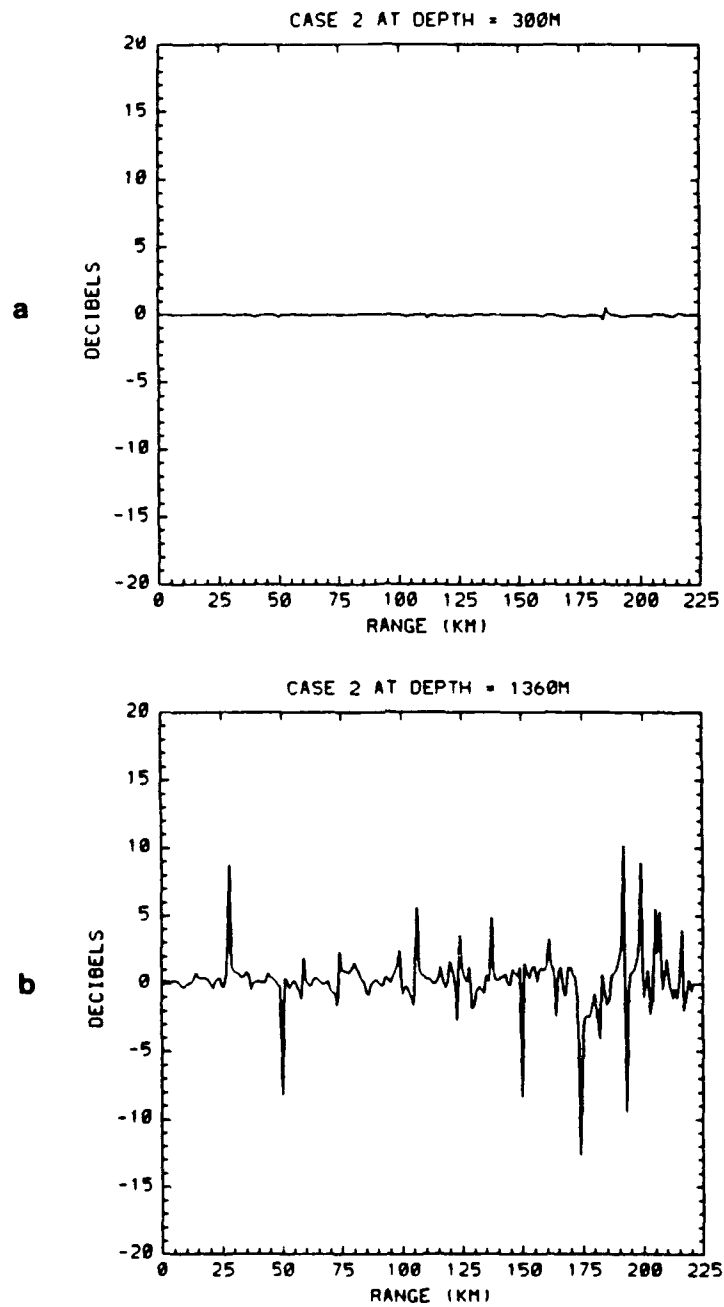


Figure 3.30: Differences in Transmission Loss Between the 3-D CM and Nx2-D Solutions at 300 m Depth (Figure 3.30a) and 1360 m depth (Figure 3.30b) along the Path $\theta = -45^\circ$. (Source is placed inside warm eddy for depths of 300 m (Figure 3.30a) and 1360 m (Figure 3.30b))

TRANSMISSION LOSS (3D - 2D) AT 1 DEG.

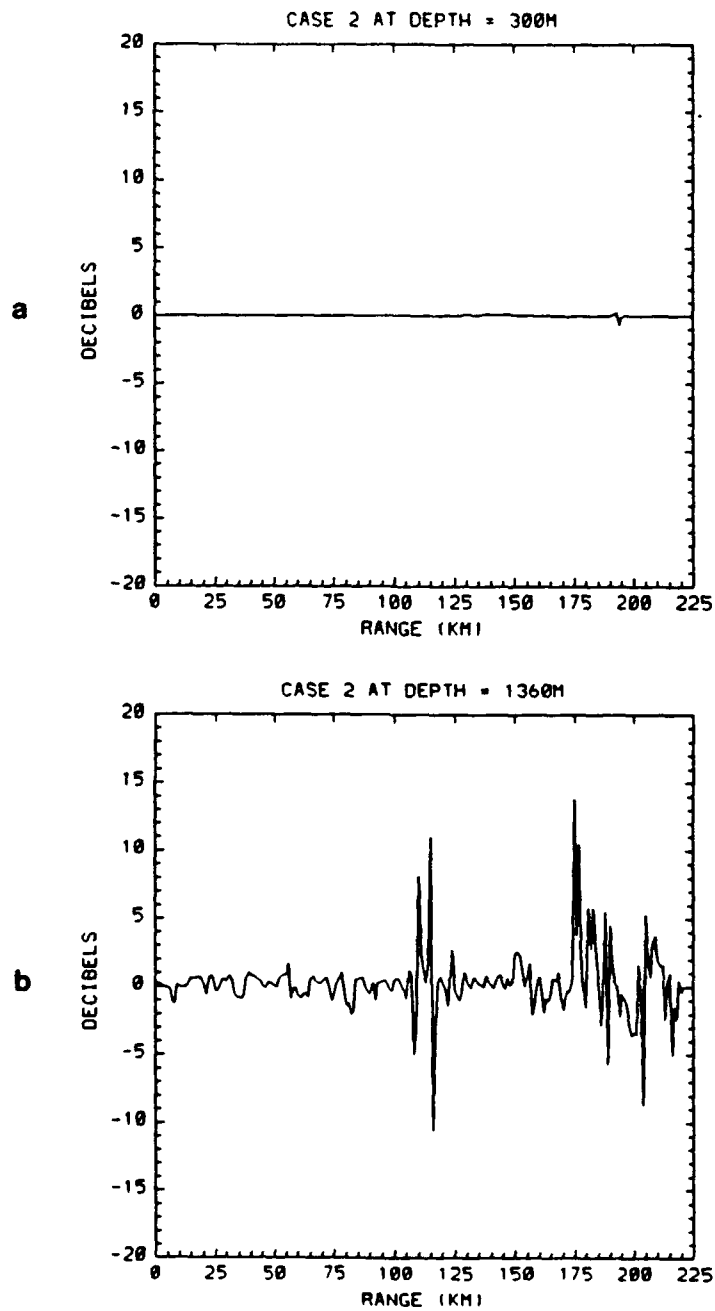


Figure 3.31: Differences in Transmission Loss Between the 3-D and Nx2-D Solutions at 300 m depth (Figure 3.31a) and 1360 m depth (Figure 3.31b) along the Path $\theta = 1^\circ$. (Source is placed inside warm eddy for depths of 300 m (Figure 3.31a and 1360 m (Figure 3.31b))

IV. CONCLUSIONS AND RECOMMENDATIONS

The 3-D CM model employed in this thesis has provided the user an opportunity to investigate the 3-D environmental effects on sound transmission in a warm eddy located north of the Gulf Stream. By placing the acoustic source at different horizontal and vertical locations within the region being investigated, thorough examination of the effects of strong sound speed gradients on underwater sound propagation is possible. Results obtained from the 2 case studies (Case 1: Source outside of warm eddy; Case 2: Source inside of warm eddy) offer the following conclusions for a 50 Hz sound source:

1. Sound propagation through the warm eddy region encounters significant horizontal refraction and acoustic mode coupling. The ability of the 3-D model coupled with the predicted sound speed field provided by HOOM has made it feasible to study these two important physical mechanisms in this region.
2. Although the CM model offers precision in the computation of sound propagation through this mesoscale ocean field, on the VAX 8250 it requires tremendous computer execution time and core storage. It is therefore advantageous to investigate the regimes for which the "approximate" models are valid in order to save computer time.
3. Mode coupling is most significant in Case 2 (particularly for the paths crossing the core of the warm eddy) due to strong radial sound speed gradients. Significant horizontal refraction along edges of the warm eddy and along a small section of the Gulf Stream front regions of strong transverse gradient are observed in Case 1.

4. Since the 3-D adiabatic approximation solution does not model mode coupling, significant errors in amplitude are found in Case 2, particularly at higher modes and at shallow source depth away from the SOFAR axis. The 3-D adiabatic approximation model generally breaks down in locations in Case 1 where large radial sound speed gradients are observed.
5. In complete contrast, the error in the Nx2-D approximation model is sensitive to the transverse sound speed gradients. For modes propagating parallel to the edges of the warm eddy, the large transverse sound speed gradients cause some phase changes. However, since the model contains the physics of mode-mode coupling, it gives accurate amplitudes everywhere in the warm eddy region.
6. Overall, the use of the adiabatic approximation for predicting transmission loss inside the core ring must be withheld since the neglect of mode coupling produces significant errors when strong radial sound speed gradients are observed. On the other hand, the Nx2-D approximation model appears to produce negligible error, particularly for a shallow source depth because low modes suffer more horizontal refraction than high modes.

While the promise of accurate acoustic prediction offered by the 3-D CM model is without question, there are still some problems. These include the amount of computer time required to run the model and core storage requirement. These two issues are of obvious concern for Navy applications because of the cost involved and time delays. Several improvements and further studies remain to be done. The algorithms for the numerical integration/iteration of the differential equations governing the complex envelopes need to be re-examined to optimize computer run time. Future research should include continuation of the model parameter studies for various acoustic frequencies,

source and receiver depths, and range of propagation, as well as study of the 3-D CM model sensitivity to spatial resolution of the sound speed input field.

APPENDIX A

IMPLEMENTATION OF CHIU-EHRET COUPLED MODE MODEL IN A VAX 8250

The CM model was originally developed on a VAX 8800. Due to the core size of the VAX 8250 used for this study, the original algorithm was modified. The computer implementation of this algorithm to study underwater sound propagation north of the Gulf Stream was accomplished in nine stages.

The first stage entails interfacing the acoustic CM model with the HOOM to compute the eigenvalues, k_n , and the eigenmodes, Z_n , using a centered finite difference approximation [Ref. 13]. The eigenvalues and the eigenmodes are then determined by the QR algorithm and method of backward substitutions [Ref. 13] respectively.

Two domains were chosen to investigate the effects of the ocean mesoscale variability north of the Gulf Stream on sound propagation.

- Case 1: A 50 Hz source is placed outside a warm eddy.
- Case 2: A 50 Hz source is placed inside a warm eddy.

In the second stage, the derivatives of the acoustic mode wave numbers are computed in Cartesian coordinates using a bi-cubic spline and then transformed into cylindrical derivatives.

In the third stage, the dimensional array size of the eigenmodes is rearranged and modified to accommodate the core storage requirements. This is achieved by writing an additional algorithm to fit the CM model to the core size of the VAX 8250.

In the fourth stage, the normal mode functions are used to compute the coupling coefficients, γ_{mn} , β_{mn} , and B_{mn} .

The terms k_n , γ_{mn} , β_{mn} , and B_{mn} are now defined over a rectangular grid containing a partial circle of radius 220 km centered at the source location. In the fifth stage, these terms are interpolated (bi-cubic spline again) to each radial integration path. Cubic (radial) splines of these terms are then calculated for each integral path needed for the calculation of the complex mode envelopes.

In the sixth stage, the coupling coefficient and cumulative wave number splines are rearranged so that they are grouped by individual angle in order to minimize storage requirements.

In the seventh stage, each individual radial path is integrated to give the complex envelope amplitude, U_n . Backscattering and the effects of horizontal sound speed variation near the source are neglected in the calculation [Ref. 13].

In the eighth stage, the acoustic pressure resulting from a point source is computed by summing all modes to estimate the intensity of the acoustic field and the propagation loss values.

In the last stage, output data are plotted using NCAR GRAPHICS subroutines.

In each of the stages 1 through 5, there are questions concerning the sensitivity of the acoustic CM model to horizontal and vertical resolution of the input sound speed field. These questions are essentially numerical analysis concerns and are not studied in this thesis. Suffice to say, the depth and range sampling must be fine enough to allow sufficiently accurate numerical solutions of the differential equations governing the depth and range functions of the acoustic wave field. For details regarding the numerical procedures used by Chiu and Ehret to compute the acoustic field, readers are advised to consult References 13, 15, and 16.

LIST OF REFERENCES

1. Pekeris, C. L., "Theory of Propagation of Explosive Sound in Shallow Water," *Propagation of Sound in the Ocean*, Geol. Soc. Am. Mem., 27, 1948.
2. Pierce, A. D., "Extension of the Method of Normal Modes to Sound Propagation in an Almost-Stratified Medium," *J. Acoust. Soc. Am.*, 37, pp. 19-27, 1965.
3. Milder, D. M., "Ray and Wave Invariants for SOFAR Channel Propagation," *J. Acoust. Soc. Am.*, 46, pp. 1259-1263, 1969.
4. Desaribies, Y., Chiu, C.-S., and Miller, J., "Acoustic Mode Propagation in a Range-Dependent Ocean," *J. Acoust. Soc. Am.*, 80 (4), pp. 1148-1160, 1986.
5. Weston, D. E., "Horizontal Refraction in a Three Dimensional Medium of Variable Stratification," *Proc. Phys. Soc.*, London 78, pp. 46-52, 1960.
6. Weston, D. E., "Guided Propagation in a Slowly Varying Medium," *Proc. Phys. Soc.*, London 73, pp. 365-384, 1959.
7. McDaniel, S. T., "Parabolic Approximations for Underwater Sound Propagation," *J. Acoust. Soc. Am.*, 58, pp. 1178-1185, 1975.
8. DeSanto, J. A., Perkins, J. S., and Baer, R. N., "A Correction to the Parabolic Approximation," *J. Acoust. Soc. Am.*, 64, pp. 1664-1666, 1978.
9. Spofford, C. W., *A Synopsis of the AESD Workshop on Acoustic Propagation Modeling by Non-Ray Tracing Techniques*, AESD Tech. Note TN 7305, Acoustic Environmental Support Detachment, Office of Naval Research, Arlington, Virginia, 1973.
10. Jensen, F. and Krol, H., *The Use of the Parabolic Equation Method in Sound Propagation Modeling*, SACLANTCEN Memorandum SM-72, La Spezia, Italy, 1975.
11. Tappert, F. D., *Selected Applications of the Parabolic Equation Method in Underwater Acoustics*, International Workshop on Low-Frequency Propagation of Noise, Woodshole, MA, 15-19 October 1974, (U.S. GPO, Washington, D.C.), Vol. 1, pp. 155-197, 1977.
12. Perkins, J.S. and Baer, R. N., "An Approximation to the Three-Dimensional Parabolic-Equation Method for Acoustic Propagation," *J. Acoust. Soc. Am.*, 72 (2), pp. 515-522, 1982.
13. Chiu, C.-S. and Ehret, L. R., "Computation of Sound Propagation in a Three-Dimensionally Varying Ocean: A Coupled Normal Mode Approach," *Computational Acoustics*, Vol. 1, pp. 187-202, ©IMACS, 1990.

14. Robinson, A. L., and Walstad, L. J., "The Harvard Open Ocean Model: Calibration and Application to Dynamical Process, Forecasting, and Data Assimilation Studies, *J. Applied Num. Math.*, 3, pp. 89-131, 1987.
15. Hull, T. E., Enright, W. H., and Jackson, K. R., *User's Guide for DVERK - A Subroutine for Solving Non-Stiff ODE'S*, TR No. 100, Department of Computer Sciences, University of Toronto, 1976.
16. Acton, F. S., *Numerical Methods That Work*, Harper and Row Publishers, 1970.

INITIAL DISTRIBUTION LIST

	No. of Copies
1. Defense Technical Information Center Cameron Station Alexandria, Virginia 22304-6145	2
2. Library, Code 52 Naval Postgraduate School Monterey, California 93943-5002	2
3. Professor Ching-Sang Chiu, Code 68Ci Department of Oceanography Naval Postgraduate School Monterey, California 93943-5100	2
4. Professor Laura L. Ehret, Code OC/Eh Department of Oceanography Naval Postgraduate School Monterey, California 93943-5100	2
5. Library Scripps Institute of Oceanography University of California, San Diego La Jolla, California	1
6. Chairman, Department of Oceanography, Code OC/Co Naval Postgraduate School Monterey, California 93943-5100	1
7. Library Naval Oceanography Office Stennis Space Center, Mississippi	1
8. Oceanography of the Navy, OP 095 Pentagon Washington, D.C. 20350-2000	1

9. Jacqueline M. Binhlam
12 Chelsea Court
Annapolis, Maryland 21403

2